ADVANCED COMPUTATIONAL NANOMECHANICS

Edited by

Nuno Silvestre

University of Lisbon
Portugal

WILEY

This edition first published 2016

Registered office
John Wiley & Sons Ltd, The Atrium, Southern Gate, Chichester, West Sussex, PO19 8SQ, United Kingdom

Library of Congress Cataloging-in-Publication Data

Advanced computational nanomechanics / edited by Nuno Silvestre.
pages cm
Includes bibliographical references and index.
ISBN 978-1-119-06893-8 (cloth)
1. Nanotechnology–Mathematics. 2. Nanoelectromechanical systems–Mathematical models.
3. Nanostructures–Mathematical models. 4. Micromechanics–Mathematics. I. Silvestre, Nuno, editor.
T174.7.A385 2016
620′.5–dc23

2015035009

A catalogue record for this book is available from the British Library.

Typeset in 10/12pt TimesLTStd by SPi Global, Chennai, India

1 2016

8

Mechanical Characterization of 2D Nanomaterials and Composites

Ruth E. Roman[1], Nicola M. Pugno[2,3,4] and Steven W. Cranford[1]

[1]*Department of Civil and Environmental Engineering, Northeastern University, Boston, MA, USA*

[2]*Department of Civil, Environmental and Mechanical Engineering, University of Trento, Trento, Italy*

[3]*Centre of Materials and Microsystems, Bruno Kessler Foundation, Trento, Italy*

[4]*School of Engineering and Materials Science, Queen Mary University, London, UK*

8.1 Discovering 2D in a 3D World

The remarkable emergence of nanotechnology has made flourish new possibilities for the characterization of nanomaterials. These small-sized structures have at least one dimension in the nanoscale (<100 nm) and can be categorized according to their dimensionality as zero-dimensional (0D), one-dimensional (1D), two-dimensional (2D), and three-dimensional (3D) materials (Figure 8.1(a)–(d)). Herein, we focus in 2D nanostructures.

Intuitively, one can easily discern the difference between 2D and 3D objects: restrict the size of a material volume to its length and width alone and reduce to zero its height. From a materials science or engineering perspective, a reduction in dimensions necessarily changes how a system is both described and characterized. Yet our own minds are accustomed to visualization in 3D – what consequences occur when a material is constrained to two dimensions poses intriguing questions. Over 100 years ago, a simple thought experiment considered life restricted to two dimensions – a hypothetical "flatland." The novel *Flatland: A Romance of Many Dimensions* is an 1884 satire by the English author Edwin Abbott Abbott. The book used the fictional (and limited) 2D world of "Flatland" to comment on the hierarchy of Victorian culture, but the novel's more enduring contribution is its examination of *dimensions*. The story describes a 2D world occupied by geometric figures, while the narrator (himself a lowly square) guides the readers through some of the implications of planer life. The square

Advanced Computational Nanomechanics, First Edition. Edited by Nuno Silvestre.

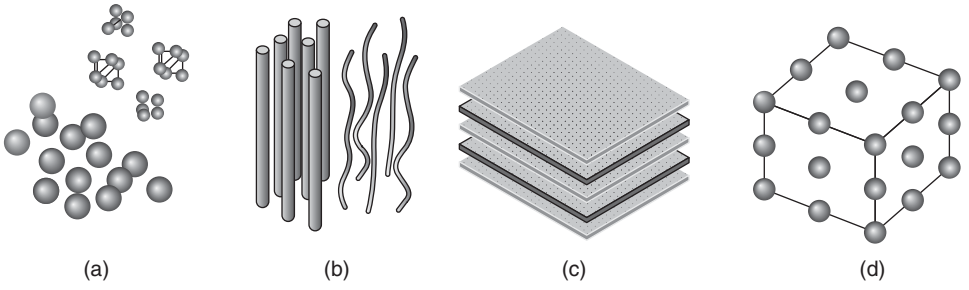

Figure 8.1 Dimensional classification of nanomaterials. (a) 0D with all dimensions in the three directions are in the nanoscale ($\leq 10^{-9}$ m). Examples of this kind are nanoparticles, quantum dots, and clusters. (b) 1D where one dimension of the nanostructure will be outside the nanometer range. Nanorods, nanotubes, and nanofibers are included in this classification. (c) 2D with two dimensions outside the nanometer range. These include different types of thin films and plates. (d) 3D with all dimensions outside the nanoscale. Bulk amorphous materials and materials with a nanocrystalline structure are included in this category

is visited by a 3D sphere, which he cannot comprehend, and only observes in discrete circles of varying sizes, for example, 2D cross sections of the sphere. The 2D materials we discuss herein would be very comfortable in Flatland – having length and width prescribed by a 2D atomic crystallinity, but constrained to a plane (with minor deviations). Moreover, like the square observing the sphere in Flatland, three dimensions of such materials can be imagined (and ultimately experimentally achieved) by grouping discrete "slices" of the 2D structures in multilayer composite systems. However, this typically does not change the 2D nature of the materials. Thus, in order to understand such materials, we are limited to 2D perspectives – a *molecular flatland*. Unlike the poor square in Abbott's novel, however, 2D materials exist in the 3D world, but have only been a recent discovery.

In 2004, a one-atom thickness monolayer of carbon atoms was isolated through relatively simple mechanical tape exfoliation of graphite [1], quietly heralding an era of 2D materials. Novoselov and Geim successfully produced the first single-layered 2D material, graphene, an achievement that granted both of them the Noble prize in Physics in 2010. Its exceptional electrical properties, potential in electronic, structural and thermal applications, and mechanical and chemical stability has suggested graphene to be one of the most remarkable structure in existence. Of course, all these superlatives mean that it has plethora of promising applications. Since then, the potential of other atomistically 2D materials has created a new paradigm of Materials Science. As graphene itself has shown, the properties of 2D structures can be astounding, and monolayers of crystals such as hexagonal boron nitride (hBN) or molybdenum disulfide could be just as mind blowing as graphene. They possess a high degree of anisotropy with nanoscale thickness and infinite length in other dimensions, exhibit great potential in applications such as energy storage and conversion systems, and hold enormous promise due to its unique functionalities and properties, which are not found when the material is in its bulk form. In order to be successful in future applications, the behavior of such materials subject to load must be fully understood, including limits in deformation and strength, and ultimate failure response. In addition, nanocomposites reinforced with 2D nanolayers have become of great interest due to their potential applications. These composite materials, in which the

matrix material is reinforced by one or more nanolayers in order to improve performance properties, commonly use polymers, ceramics, and metals as matrix [2], and form a 3D arrangement.

This chapter reviews 2D nanomaterials and composites from the standpoint of their mechanical properties. We discuss first the state of the art for graphene-related nanomaterials, and then we focus in some of the more important experimental and analytical tools used for the characterization of nanomaterials, and the different approaches used to characterize the mechanical properties and behavior of an atomistic system, such as strength, stiffness, and failure. Finally, we focus in multilayers and nanocomposites and the challenges of mixing different materials in the context of mechanical properties.

8.2 2D Nanostructures

The study of 2D nanostructures has witnessed an increasing development over the past several years due to the success of graphene and its remarkable characteristics. These novel materials have extraordinary properties and promising applications. Recently, several works have been published on graphene-like materials, including silicene, germanene, and molybdenum disulfide, which have been studied and designed from both experimental and computational sides, allowing to predict interesting properties and establishing new fabrication methods. Here, we briefly review some of these fascinating 2D nanostructures that represent a new breakthrough in materials science.

8.2.1 Graphene

The most prominent 2D nanostructure is graphene, which is a honeycomb arrangement of sp^2-hybridized carbon atoms that has almost the same per-atom crystal energy as diamond (sp^3 structure) (Figure 8.2(a) and (b)). As each graphene carbon has only three bonds instead of four for diamond, the graphene C–C bonds are about 25% stronger [3]. Thus, in plane, it is the strongest material ever measured, and is both chemically stable and inert. Graphene has a particular electronic structure, due to the presence of a Dirac cone in its electronic band structure, which makes graphene conducts electricity better than any other known material at room temperature [4]. In addition, it does not show a band gap, but the density of states is zero at the Fermi level [3]. Today, graphene can be produced by several methods that depend on the quality and dimension of the material to be obtained. Furthermore, we can list other exceptional properties of graphene, such as high specific surface area, high carrier mobility, high thermal conductivity, half-integer quantum Hall effect, and ambipolar electric field effect.

Several researchers have determined the mechanical properties of a single layer of graphene, and it has been reported to have the highest elastic modulus and strength, compared with other materials. The Young's modulus of a graphene sheet is reported on the order of 1 TPa (335 N/m) using different techniques including Raman spectroscopy and AFM [5, 6]. Similarly, computational and experimental works report that the ultimate stress for single layer of graphene is 130 GPa, for an approximate ultimate strain of 20%–25% strain [5]. The bending modulus for graphene has been calculated as well, based on *ab initio*, molecular dynamics (MD) and other techniques resulted in values in the order of 1.5 to 2.1 eV for monolayer graphene and approximately 130 eV for bilayer graphene sheets [7].

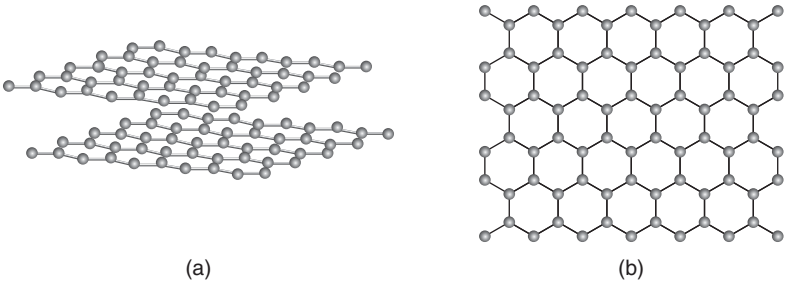

Figure 8.2 Atomic structures of (a) graphite and (b) graphene

8.2.2 Graphynes and Graphene Allotropes

The recent advent of graphene has motivated further investigation of similar 2D systems, including all-carbon allotropes of graphene, as well as other 2D crystals. In this group, we highlight the family of graphynes. The graphyne family is an all-carbon allotrope of graphene, in which the framework in general consists of characteristic hexagonal carbon rings connected by acetylenic linkages (single- and triple-bond, Figure 8.3(a) and (b)), which is made up of a variation of the sp^2 carbon motif-forming graphene. In this group, we highlight graphdiyne, a member of the graphyne family proposed by Haley et al. in 1997 [8] with characteristic diacetylenic links. Presently, thin films of graphdiyne have been successfully fabricated on a copper (Cu) substrate by a cross-coupling reaction using hexaethynylbenzene [9], suggesting the future feasibility of extended graphyne structures. In the process, the Cu foil serves as both the catalyst and substrate for growing the graphdiyne films.

Although the mechanical performance of graphdiyne is noticeably inferior to graphene, the graphdiyne structure is predicted to be the most synthetically approachable, and the most stable diacetylenic non-natural carbon allotrope [9]. It has been found that graphdiyne exhibits semiconductive characteristics and, advantageously, the natural band gap in graphdiyne, which can vary as a function of directional anisotropy, is similar to that of silicon and makes it the possible supplant material to silicon electronic devices. The possible applications of graphdiyne sheets and nanoribbons due to its promising properties include nanoelectronics, energy storage, anode materials in batteries, for hydrogen storage, or as membranes for gases separation [10].

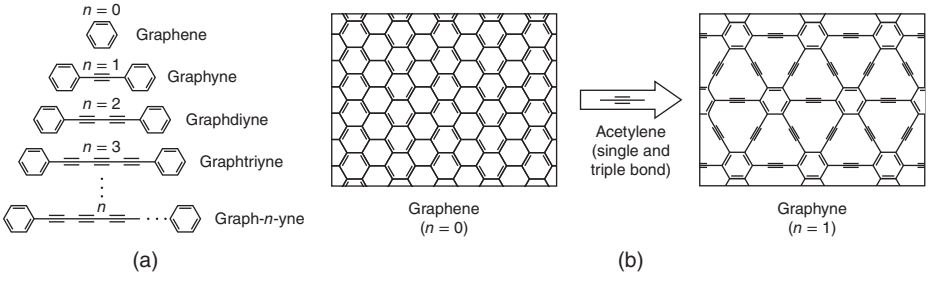

Figure 8.3 (a) Classification of graphyne family. (b) Schematic of graphene to graphyne

Table 8.1 Mechanical properties for extended graphynes [11]

Structure	n	Reclined chair direction			Zigzag direction		
		E (GPa)	σ_{ult} (GPa)	ε_{ult} (%)	E (GPa)	σ_{ult} (GPa)	ε_{ult}
Graphyne	1	532.5	48.2	8.2	700.0	107.5	13.2
Graphdiyne	2	469.5	36.0	6.3	578.6	45.5	8.0
Graphtriyne	3	365.0	26.8	7.7	476.7	43.7	9.9
Graphtetrayne	4	370.4	24.8	7.0	453.3	32.5	9.7

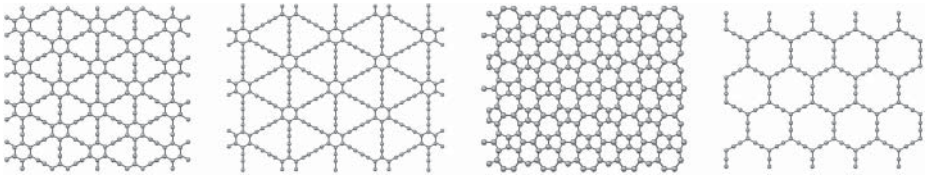

Figure 8.4 Atomic structures of graphene allotropes. (a) Graphyne, (b) graphdiyne, (c) graphene allotrope with Stone–Wales defects, (d) supergraphene

The mechanical properties of the extended graphyne family in both armchair (or reclined chair) and zigzag directions have been reported in previous studies, and are summarized in Table 8.1. A consistent degradation of the properties is observed, with the addition of acetylene linkages to the structure.

With the purpose of defining further approaches to achieve controllable manipulation of the atomic, electronic, and mechanical properties of all-carbon graphene, different graphene allotropes have been developed (see Figure 8.4(a) and (b)). An alternative approach is the introduction of variation in structure and topology of graphene, such as atomic-scale defects (Stone–Wales defects, see Figure 8.4(c)), or the substitution of the original carbon–carbon bonds in graphene by acetylene carbyne-like chains (Figure 8.4(d)) [12]. The introduction of acetylene links introduces an effective reduction in stiffness, strength, and stability, enabling the properties to predict the nanostructures properties as a function of acetylene repeats [11].

The 2D materials family is of course not limited to carbonic crystals, although similar problems are faced when attempts are made to synthesize other 2D materials.

8.2.3 Silicene

Among the various 2D crystalline structures similar to graphene is also all-silicon-based silicene. Owing to its current use in semiconductor electronics combined with a similar hexagonal graphene-like lattice, this monolayer allotrope of silicon (Si) has attracted increasing attention due to its potential compatibility with Si-based electronics. It was first mentioned in a theoretical study by Takeda and Shiraishi [13] in 1994 and then investigated by Guzman-Verri et al. in 2007, who labeled it silicene [14]. Structurally, silicene is a 2D sheet of hexagonally arranged silicon atom, analogous to graphene, but with consecutive bonds buckled out-of-plane. Unlike graphene, silicene is not stable as a perfectly planar sheet, with

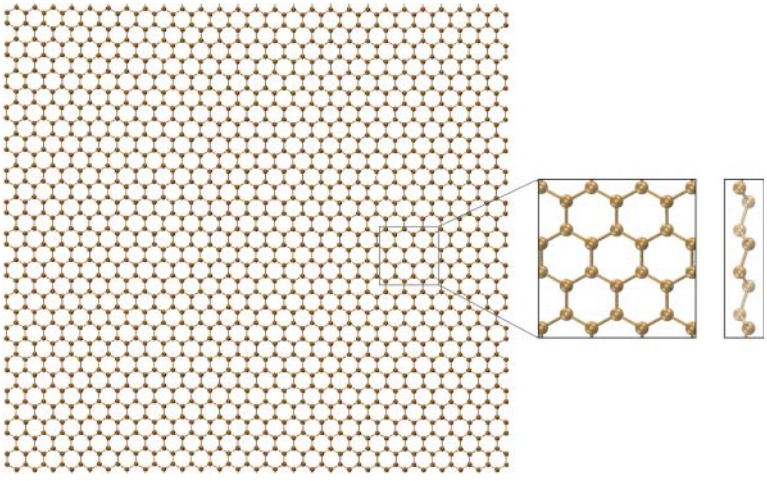

Figure 8.5 Schematic of silicene

chair-like distortions in the rings leading to ordered surface ripples and enhancing reactivity with other material surfaces. Being said, as sp^3 hybridization is more stable in silicon than sp^2 hybridization, silicene is energetically favorable as a low-buckled structure, as depicted in Figure 8.5. This buckling confers advantages on silicene over graphene because it should, in principle, generate both a band gap and polarized spin-states that can be controlled with a perpendicular electrical field [15].

The mechanical properties (in-plane stiffness and ultimate strength) of silicene in both armchair and zigzag directions, as well as the bending rigidity have been previously deduced theoretically in the literature using techniques such as MD and DFT. The in-plane stiffness in zigzag direction is reported in the range of 50–65 N/m, whereas in armchair direction the reported values of in-plane stiffness range from 59 to 65 N/m [16, 17]. The ultimate stress is reported approximately 5–8 N/m for both directions, with the corresponding value of maximum strain between 10% and 20% [16, 17]. The bending modulus has been obtained by curve fitting with energy versus curvature data points and is calculated to be approximately 38 eV. Compared with monolayer and bilayer graphene, it can be noted that this value falls between these two values. This could be due to the out of buckling structure of silicene, which creates an effective thickness and bending inertia, compared to flat graphene, which does not have this effect [16].

8.2.4 Boron Nitride

Boron nitride (BN) is another 2D nanostructure with graphene-like structure that consist of alternating boron and nitrogen atoms in a hexagonal arrangement, where boron and nitrogen atoms are bonded with strong covalent sp^2 bonds (Figure 8.6), while for multiple layers they are stacked together by electrostatic interaction and weak van der Waals forces, as in graphite. Therefore, BN layers could be peeled off from bulk BN crystal by micromechanical cleavage and used as a dielectric layer [18]. For this reason, bulk BN is commonly called white graphite, and in analogy the monolayer hBN is known as white graphene [19].

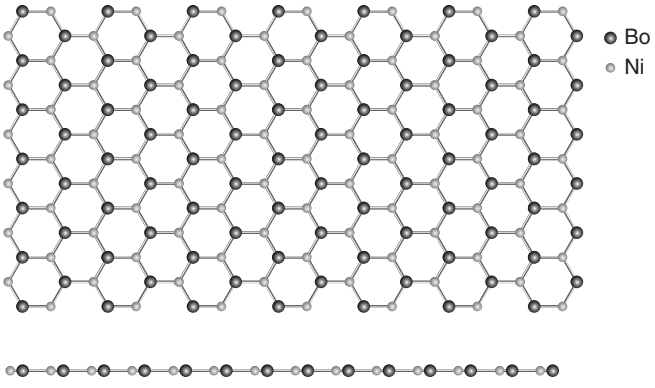

Figure 8.6 Atomic structure of boron nitride (BN)

BN, unlike graphene, is an insulator due to the difference in electronegativity, where the narrowing of the sp^2 p-bands is responsible for the loss of conductivity [18]. BN is well known for a variety of crystalline structures (cubic, rhombohedral, amorphous); however, its hexagonal layered structure is the most stable. Due to a combination of exceptional properties, from which we can highlight its high oxidation resistance, large thermal conductivity, good electrical insulation, chemical inertness, nontoxicity, apart from being environmentally friendly, this versatile inorganic compound can be used for a wide range of industrial applications, such as surface coatings, ceramic composites, lubricants, or insulators [20].

The mechanical parameters of boron nitrate have been reported in different studies using theoretical calculations such as density functional theory (DFT). The Young's modulus of single-layered hBN is about 780 GPa and is nearly independent of loading orientation. The bending rigidity is also isotropic and is about 0.95 eV. The ultimate tensile stresses are 102, 88, and 108 GPa for the zigzag, armchair, and biaxial strains, respectively [21].

8.2.5 Molybdenum Disulfide

Molybdenum disulfide (MoS_2) is an inorganic 2D material, semiconductor with hexagonal structure, and the most prominent member of the family of transition metal dichalcogenides (TMD). TMDs are representing by the formula MX_2, where $M =$ Mo, W, V, Nb, Ta, Ti, Zr, Hf, and $X =$ S, Se, Te, constituting a fascinating group of materials with an extensible range of remarkable mechanical, optical, and electronic properties and applications [19]. Structurally, it consists of three-atom-thick layers of a monatomic molybdenum plane between two monatomic sulfur planes, such as a sandwich structure (Figure 8.7), in which the atoms are bonded with strong covalent bonding, and the layers are held together by van der Waals interactions [22]. MoS_2 can be obtained easily from the bulk material using exfoliation techniques, such as graphene and BN [23].

The presence of a direct band gap in monolayer MoS_2 makes it promising for nanoelectronics and photoelectronics applications. Another special feature of this material is that the electronic structure can be tuned by varying the number of layer due to perpendicular quantum confinement effect [19]. Additionally, its functional and structural properties can

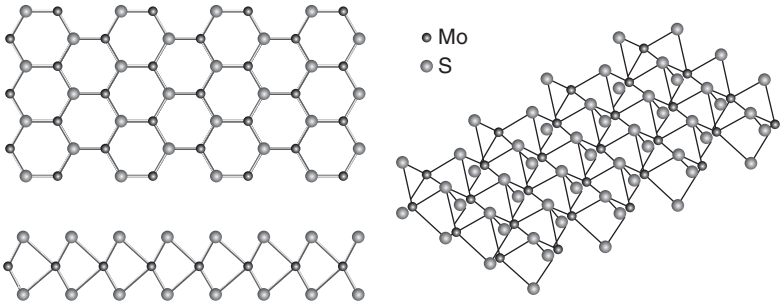

Figure 8.7 Atomic structure of molybdenum disulfide (MoS_2)

be modulated by the application of mechanical strain, electric field, surface adsorption, and defects [19, 24].

Due to the remarkable mechanical properties of MoS_2, such as large ultimate strains, resulting in high flexibility, and high strength and stiffness, the material is presented as a promising candidate for elastic energy storage for clean energy, as reinforcement in nanocomposites, and for fabrication of flexible electronic devices. Furthermore, it is environmentally friendly. Several studies report the mechanical properties of MoS_2, using DFT calculations. For a single layer of MoS_2, the Young's modulus is reported in the range of 184–270 GPa, while the ultimate strength is reported between 12 and 24 GPa [19, 24, 25].

8.2.6 Germanene, Stanene, and Phosphorene

The remarkable properties and extensive applications of carbon-based graphene have lead to the research of layered structures of the other elements in main group IV (Si, Ge, Sn, and Pb), resulting in the development of new and innovative atomic 2D nanostructures: germanene and stanene. In their stable state, these elements form a buckled hexagonal structure, unlike graphene. This is related to the nature of graphene possessing an sp^2 hybridization, whereas silicene, germanene, and stanene exhibit the sp^2–sp^3 hybridization due to their preferential state of sp^3 bonding [26].

One of these promising materials is germanene, which is the germanium analog of silicene. Based in first principled DFT calculations, Cahangirov et al. reported that the low-buckled honeycomb structure of germanium analog of graphene can be stable [27]. Trying to produce germanene, the hydrogen-terminated germanene was synthesized in 2013 from the topochemical deintercalation of calcium digermanide (CaGe2) [28]. Afterwards, Li et al. [29] have reported the successful fabrication of germanene by an annealing process after having deposited germanium onto a Pt(111) surface. As in free-standing silicene, germanene presents no band gap at the Fermi level, indicating metallic properties [3].

Two-dimensional tin, called stanene, is another versatile Group IV elemental 2D material. Stanene presents an intrinsic buckling that allows for functionalization by an out-of-plane electric field, and almost full sp^3 hybridized bonding. It also owns a slightly metallic band alignment, with massless Dirac fermions, analogous to silicene and germanene, which are excellent properties for potential nanoelectric applications [30]. Although there is a lack of

knowledge on the fundamental properties of some of these Group IV 2D allotropes, the notable correspondence in their crystal and electronic structures enables the properties of germanene and stanene to be extrapolated through relative estimations with graphene and silicene [26].

Recent theoretical studies on the in-plane stiffness of Group IV elemental layers reported an observed reduction in the stiffness with increasing atomic weights (from Si to Sn). This observation is related to the tendency of metallic bonding with increasing atomic weight that is evidenced by the increasing bond length [31].

One of the latest 2D nanostructure developed is phosphorene, which was isolated by liquid exfoliation of black phosphorus [32]. Similar to graphite, black phosphorous is made of stacked layers of phosphorene held together by weak van der Waals forces [33]. Phosphorene, such as graphene, is the elementary 2D nanolayer that composes black phosphorus crystals, but unlike graphene, it has a unique, vertically skewed/wrinkled hexagonal structure (Figure 8.8). Monolayer phosphorene is a semiconductor with a predicted direct band gap, which combined with tunability of its properties makes it an ideal candidate for nanoelectronic, optoelectronic, and photovoltaic applications [26].

It should also be noted that chemical functionalization, especially hydrogenation, is also being used to develop new 2D nanomaterials, such as germanane. The hydrogenated counterpart of graphene is graphane, a fully saturated 2D hydrocarbon with sp^3 hybridized bonds that opens up. Graphane is an insulator and lacks the Dirac cone of graphene [34]. Hydrogenation process can lead to the deterioration of graphene mechanical properties, such as Young's modulus and shear modulus due to membrane shrinkage and extensive membrane corrugation caused by functionalization [35]. Also under study is silicane, the fully hydrogenated version of silicene, which is a wide-band-gap semiconductor that is projected as a promising potential candidate not only for nanoelectronic applications but also for hydrogen storage [36]. For hydrogenated BN, the hybridized states of boron or nitrogen atoms change from sp^2 into sp^3. Hydrogenation opens a band gap in graphene, but it reduces the band gap of BN sheets. Silicane, the fully hydrogenated version of silicene, is a wide-band-gap semiconductor that is projected as a promising potential candidate not only for nanoelectronic applications but also for hydrogen storage [19].

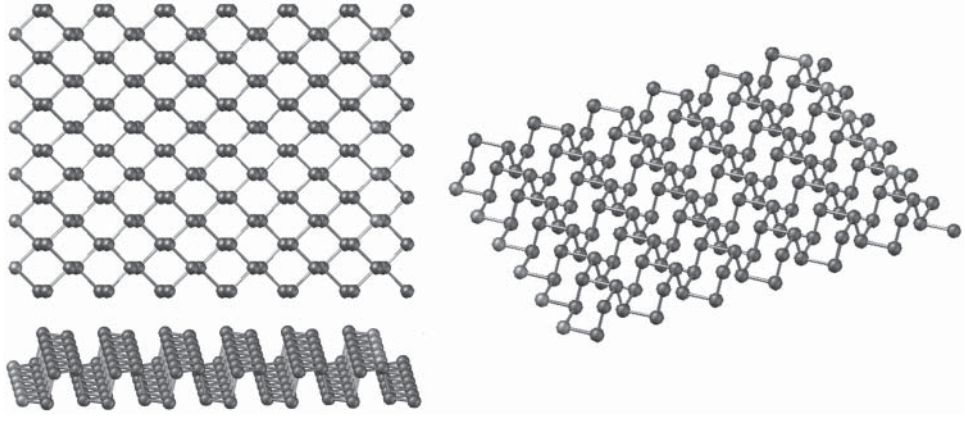

Figure 8.8 Atomic structure of phosphorene

8.3 Mechanical Assays

There are two basic approaches to investigate the mechanical performance of a nanomaterial: experimental and computational modeling. The difference between these two methodologies is that modeling presents how materials *should* behave, experimentation presents how materials *do* behave. Both methodologies face challenges when applying to study nanostructures. On the one hand, experiments should be capable to identify, measure, and manage the different variables on the system; on the other hand, modeling methods must deal with assumptions, constraints and boundary conditions, unknowns, and the complexity of real material structure and environments. While experimental approaches are necessary to characterize emerging 2D materials, we concentrate primarily on computational methods herein. Due to the precise control of material geometries and boundary conditions, computational methods are advantageous when exploring theoretical mechanistic models, requiring less assumptions and conditions than experimental techniques. Ultimately, both models and experiments broadly contribute to the understanding of the nanostructures behavior.

8.3.1 Experimental

Mechanical characterization through experimental methods represents a successful approach to study the behavior and properties of 2D nanostructures. Various experimental techniques are being used to image single layer or multilayers of 2D structures such as optical microscope, atomic force microscopy (AFM), scanning electron microscopy (SEM), and transmission electron microscopy (TEM). Probing the atomic structure of 2D materials is a demanding task due to the small sample size and the choice of technique on the measurement requirements. Often, a combination of two or more techniques completes the characterization of nanomaterials, allowing the fast estimation of parameters as thickness distribution and facilitating their observation and identification [19].

One of the most used methods for carrying out experimental measurements of mechanical properties in 2D nanostructures is scanning probe microscopy (SPM), which is a family of methods that use a sharp probe of nanometer dimension to detect changes in the material surface structure on the atomic scale [37]. SPM provides 3D real space images and enables spatially localized measurements of structure and properties. AFM is one of the prominent members of the SPM family, which can produce topographic images of a surface with atomic resolution in all three dimensions, moreover, combining with appropriately designed attachments, such as nanoindentation, and allowing its use in measuring the mechanical properties such as Young's modulus and hardness of various types of materials [38].

AFM has been used with multilayered graphene sheets in static deflection tests to measure the effective spring constants [39]. Another approach was employed to probe graphene sheets [5, 40], hBN [41], and monolayer MoS_2 suspended over circular holes [42] (Figure 8.9), which yielded the Young's modulus, bending rigidity, and breaking strength by comparing the experimental data to a continuum plate model [43]. The requirement that the material to be suspended translates into a significant limitation because of the use of nanoindentation method with some 2D nanostructures. The presence of a substrate, over which the nanostructure may be either deposited or directly grown epitaxially (e.g., silicene over silver [44], graphdiyne over copper [9]), makes it hard to separate the intrinsic mechanical properties of the nanolayer from that of the substrate from the nanoindentation measurements [40].

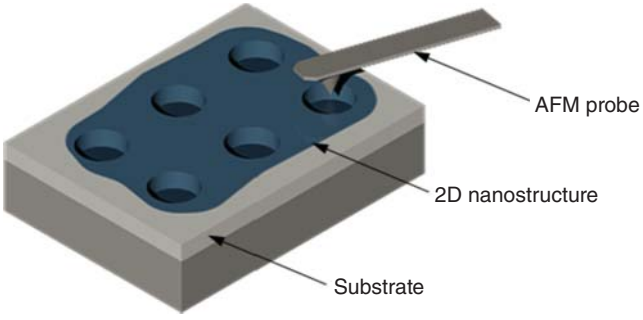

Figure 8.9 Schematic of an indentation experimental setup showing a nanostructure on substrate, suspended over open holes. The mechanical properties are probed by deforming and breaking the resulting suspended free-standing sheet with an atomic force microscope (AFM)

Raman spectroscopy is a vibrational technique that provides access to information relating to the lengths, strengths, and arrangements of chemical bonds in a material, but the method is not highly sensitive to information such as chemical composition [40]. Raman technique uses the interrogation of bond vibrations by optical spectroscopy and provides information about crystallite size, the presence of sp^2–sp^3 hybridization, the introduction of chemical impurities, the optical energy gap, elastic constants, defects, edge structure, strain, number of layers, and mechanical and structural properties for single or multilayer structures, both freestanding or on a substrate [45, 46]. Raman spectroscopy has been widely used in mechanical characterization of graphene layers [40].

Other useful experimental technique with broad applications with 2D nanostructures is TEM, in which a beam of electrons is transmitted through the sample, interacting with the specimen as it passes through [47]. The scattering processes experienced by electrons during their passage through the specimen determine the kind of information obtained, such as the layer sizes, the elemental composition, the nature of crystallinity, and interlayer stacking relationships [38, 48].

8.3.2 Computational

The advancement of computational and processing power in recent decades has rapidly paced the theoretical investigations on various materials ranging from bulk to nanomaterials. Computational techniques such as MD, DFT, and Monte Carlo simulations provide advantageous understanding to elucidate and study the nanoscale phenomena. Moreover, computational methods have become an indispensable tool to the investigation of material systems, complementing the experimental analysis for conducting materials design and property prediction.

MD is a simulation technique that consists of numerically solving the classical equations of motion for a group of atoms, in which the motion of each atom in the material is characterized by its position, velocity, and acceleration. The molecular dynamic method encompasses five basic steps: definition of initial conditions (initial temperature, number of particles, density, time steps, etc.), identify initial positions and velocities of the system particles, integration of Newton's equations of motion, calculation of the force acting on every particle, and

computation of the average of measured quantities. Each atom is considered as a classical particle that obeys Newton's laws of mechanics. The only physical law that is used to simulate the dynamical behavior of the atoms is Newton's law, along with a definition of how atoms interact with each other. Those interactions are the so-called interatomic potentials or force fields that describe attractive and repulsive forces in between pairs or larger groups of atoms [49].

DFT, based on quantum theories of electronic structure, is currently the most commonly employed quantum mechanics method, which has evolved into a powerful tool for computing electronic ground-state properties of a large number of nanomaterials. The entire field of DFT method relies on the theorem that the ground-state energy of a many-electron system is a unique and variational functional of the electron density, and this conceptual proposal is implemented in a mathematical form to solve the Kohn–Sham (KS) equations [19]. We note that, due to the system size constraints of DFT, in this chapter we focus on the MD approaches to mechanical characterization of 2D materials, which are more versatile in implementation. Being said, DFT and other quantum-level approaches have a degree of accuracy unattainable by the potential formulations of MD. Moreover, when analytical potentials are available, the effect of various types of interactions can be investigated by switching off, or modifying, the corresponding potential energy terms, being able to probe our understanding of the studied problems. Being said, prudence is necessary when selecting any approach to characterize such systems, with understanding of both the advantages and limitations of any method.

8.4 Mechanical Properties and Characterization

Atomistic simulations have proved to be a unique and powerful way to investigate the mechanical properties of 2D systems at a very fundamental level, and provide a means to investigate complex systems with unparalleled control and accuracy. MD has evolved as a suitable tool for elucidating the atomistic mechanisms that control deformation at the nanoscale and for relating this information to macroscopic material properties. Mechanistic behavior, function, and failure are directly linked to distinct atomistic mechanics and require atomistic and molecular level modeling as an indispensable tool for studying 2D materials [50]. The implementation of full atomistic calculations of mechanical test cases by classical MD has been used successfully to derive a simplified set of parameters to mechanically characterize monolayer systems such as graphene, simple graphyne, and silicene, which are in good agreement with the experimental data as far as available. The atomistic-level characterization techniques described herein are equally applicable to different structures and can be immediately applied to various 2D material geometries.

One of the most logical approaches to characterize the mechanical properties and the behavior of an atomistic system is to emulate the testing procedures and measurement of the macroscale material, including tensile and compression tests, three-point bending tests, torsion, and so on. For example, a small model system can be constructed as a computational "test specimen" with direct control over the loading and boundary conditions, from which the specimen can be subject to various testing procedures and mechanical properties directly determined. The dominance of specific mechanisms is controlled by geometrical parameters, the chemical nature of the molecular interactions, as well as the structural arrangement. Such response-based approaches are advantageous when there is inherent difficulty in defining traditional elastic "properties" such as bending stiffness or Young's modulus.

8.4.1 Defining Stress

To obtain the maximum strength or ultimate stress (along with corresponding extensibility or ultimate strain) for different 2D nanostructures, the most direct approach is to apply a uniaxial tensile strain along the representative directions in the material, analogous to a traditional macroscopic tensile coupon test. One just need to extract the corresponding stress though atomistic measures – this is typically accomplished using *virial stress* (following the *virial theorem* of Classius, 1870, which relates the average over time of the total kinetic energy of a stable system of constant particles bound by potential forces). The virial stress is commonly used to find the macroscopic (continuum) stress in MD computations [51, 52].

Mechanical stress is the measure of the internal forces acting within a deformable body and is inherently a continuum concept. In the molecular interpretation there is no continuous deformable body, but a set of discrete atoms. To reconcile this fact, we fundamentally define material stress as the change in free energy density is a function of material strain, or

$$\sigma_{ij} = \frac{\partial u}{\partial \varepsilon_{ij}} \tag{8.1}$$

where σ_{ij} is the component of stress induced by a strain, ε_{ij}, and the free energy density, u, is defined as the energy per unit volume (the indices i and j refer to the basic vectors of an arbitrary coordinate system). The formulation of stress in terms of energy landscape is convenient, as it is also a common description of atomistic systems in terms of potential energy functions or force fields, where

$$u = \frac{1}{\Omega}\sum\nolimits_{a\in\Omega} \phi_a(\chi) \tag{8.2}$$

in which Ω is the considered system volume, a the atoms within that volume, and ϕ_a the potential energy function dependent on some state variable χ (the total strain energy $U = u\Omega$). The continuum stress interpretation of atomic force fields is important, allowing the intensity and nature of internal interactions in materials to be measured and equated with macroscopic metrics (such as Young's modulus).

In order to obtain the atomistic–molecular counterpart of the stress tensor (as defined in Eq. (8.1)), we consider a small sample volume, Ω, of an atomistic system.[1] This sample volume contains N atoms, described by positions $r_i^{(a)}$ for $a \in 1, \ldots, N$. The components of the position vector can be denoted by $i = 1, \ 2, \ 3$ in 3D space (e.g., $r_1^{(a)}, r_2^{(a)}, r_3^{(a)}$). The number of atoms is large enough to allow an adequate definition of elastic field (stress and strain) in the region. The virial stress approach allows us to determine the components of the macroscopic stress tensor by considering both the kinetic energy of the atoms and the interatomistic forces through the virial components, S_{ij}, in the representative volume Ω, where

$$S_{ij} = \sum\nolimits_{a\in\Omega}\left[-m^{(a)}v_i^{(a)}v_j^{(a)} + \frac{1}{2}\sum\nolimits_{b\in\Omega}\left(\left(r_i^{(a)} - r_i^{(b)}\right)F_j^{(ab)}\right)\right] \tag{8.3}$$

which generates the six components of the symmetric stress–volume tensor, S_{ij}, where $m^{(a)}$ is the mass of particle "a," $v_i^{(a)}$ and $v_j^{(a)}$ are the velocities in the ith and jth vector component basis, $r_i^{(a)} - r_i^{(b)}$ denotes the distance between particle "a" and atom "b" along the ith vector component, while $F_j^{(ab)}$ is the force on particle "a" exerted by particle "b" along the jth vector

[1] Assumed elastic and following the derived continuum laws as $\Omega \to \infty$.

component (defined by the interatomistic potential, $\phi_a(\chi)$). We observe that the velocity v_i of each atom is composed by a term corresponding to an effective macroscopic drift. As a sum of both the kinetic energy and directional force of the potential, the virial can be (colloquially) considered a kind of "directional strain energy," akin to the strain energy, U.

To reduce random fluctuations, in addition to averaging over the representative spatial volume, Ω, it is recommended to average further over small time interval around the desired time of the stress. We introduce the time average:

$$\langle f(t)\rangle = \lim_{\tau\to\infty}\left[\frac{1}{\tau}\int_0^{\tau} f(t)\,dt\right] \tag{8.4}$$

The total stress can be calculated as

$$\sigma_{ij} = \langle S_{ij}\rangle\Omega^{-1} \tag{8.5}$$

We note that the virial stress defined as in Eq. (8.5) is equivalent to Cauchy stress only in the framework of linear approximation. However, the virial stress can easily be calculated regardless of nonlinearity, large strains, and/or failure/fracture response, dependent on the fidelity of the atomistic potentials.

One primary advantage of the virial stress approach is that it can shed insight into the coupling of deformation modes and stress distributions in a molecular system, by simultaneously and directly evaluating all components of stress. By calculating the virial stress, any direct force–extension data (e.g., from an applied spring load) can be directly compared to the virial stress and strain along the axis of extension. If there is limited coupling (e.g., no shear modes under pure tension), the results of the virial stress–strain and the applied load–displacement should agree both qualitatively and quantitatively. Disagreement between the axial stress and "force over area" calculations can indicate either the dominance or coupling with a second-order mode of deformation, such as shearing or twist. Moreover, while per atom virial stresses may be inappropriate (in terms of an equivalence to the continuum interpretation of stress), they can be used to map a virial stress field and indicate potential localizations of high force and failure events. This can shed great insight into heterogeneous material systems to indicate any potential "weak links" [50].

Virial stress combined with explicitly applied loads and displacements are powerful tools in the determination of the mechanical properties of complex molecular systems. Ultimately, they rely on fundamental stress–strain relationships formulated by continuum theory, and effectively "translate" simulation results into representative mechanical characterization. However, some systems require a more fundamental interpretation of mechanical behavior when the system is unsuitable for applied loads or prescribed boundary conditions. For such systems, fundamental energy methods can be prescribed [50].

8.4.2 Uniaxial Stress, Plane Stress, and Plane Strain

The exemplary "strength" of 2D materials is an attractive and ubiquitous indicator of their potential in nanotechnology. Indeed, defect-free graphene is said to have an intrinsic strength high than any other material. As such, we first focus on the characterization of ultimate stress. Similar to macroscale counterparts, material strength is most commonly characterized by simply loading a representative sample until failure. Simulated uniaxial tensile tests can be

applied to a 2D material sheet by fixing the boundaries in the desired direction and deforming a unit cell by stretching along tested direction at a uniform rate (thereby inducing a uniform strain rate). It is noted that the fixed edges are free to move orthogonal to the applied strain, and measurement of transverse deformation/contraction can thus be used to determine Poisson's ratio, ν. Free edge and nonperiodic boundary conditions result in a sheet of finite size, enabling size-dependent studies if desired. Due to the relatively high ratio of edge atoms to bulk atoms in 2D materials, it has been shown that limiting the width of the system (e.g., nanosheets vs nanoribbons) can greatly affect the mechanical response [53].

As stress is fundamentally a 3D concept (undergraduates are often introduced to stress in terms of a force (1D vector) acting normal to a plane (2D surface), necessitating 3D), what is the stress interpretation of an ideal 2D system? In continuum mechanics, a material is said to be under *plane stress* if the stress vector is zero across a particular surface. When that situation occurs over an entire element of a structure (as is often the case for thin plates), the stress analysis is considerably simplified, as the stress state can be represented by a tensor of dimension two. A related notion, *plane strain*, is often applicable to very thick members, whereby strain is limited to zero in a direction, but stress is allowed. Two-dimensional materials represent a combination of both plane stress and plane strain, as neither stress nor strain can possibly be induced out of plane. To illustrate, first, we consider the uniaxial extension of an elastic system. If the extension is in the x-direction, and the material is presumed isotropic and homogeneous and within its elastic limit, then Hooke's law applies

$$\sigma_x = E\varepsilon_x \tag{8.6}$$

where σ_x is the stress, ε_x the strain, and E is the Young's modulus (e.g., uniaxial stiffness). Ultimate stress or strength can easily be taken as the maximum stress experienced prior to system failure during MD simulation.

Realizing, however, that extensions/strains in other directions are proportional to Poisson's ratio, $\nu_{ij} = -\varepsilon_i/\varepsilon_j$, the strains in three dimensions can be represented as

$$\begin{bmatrix} \varepsilon_x \\ \varepsilon_y \\ \varepsilon_z \end{bmatrix} = \frac{1}{E}\begin{bmatrix} 1 \\ -\nu_{yx} \\ -\nu_{zx} \end{bmatrix}\sigma_x \tag{8.7}$$

Similar relationships apply for stress in the other two directions, so we obtain the equations that apply to any 3D stress problem where axial strains are only considered:

$$\begin{bmatrix} \varepsilon_x \\ \varepsilon_y \\ \varepsilon_z \end{bmatrix} = \frac{1}{E}\begin{bmatrix} 1 & -\nu_{xy} & -\nu_{xz} \\ -\nu_{yx} & 1 & -\nu_{yz} \\ -\nu_{zx} & -\nu_{zy} & 1 \end{bmatrix}\begin{bmatrix} \sigma_x \\ \sigma_y \\ \sigma_z \end{bmatrix} \tag{8.8a}$$

Typically, for the case of plane stress, the condition that $\sigma_z = 0$ would be applied, whereas for plane strain, the condition that $\varepsilon_z = 0$ would be applied. These conditions result in the plane stress and plane strain formulations that can be found in any traditional elasticity text. However, for 2D materials, we can apply both conditions simultaneously, such that

$$\begin{bmatrix} \varepsilon_x \\ \varepsilon_y \\ 0 \end{bmatrix} = \frac{1}{E}\begin{bmatrix} 1 & -\nu_{xy} & -\nu_{xz} \\ -\nu_{yx} & 1 & -\nu_{yz} \\ -\nu_{zx} & -\nu_{zy} & 1 \end{bmatrix}\begin{bmatrix} \sigma_x \\ \sigma_y \\ 0 \end{bmatrix} \tag{8.8b}$$

which results in the equations:

$$\varepsilon_x = \frac{1}{E}(\sigma_x - \nu_{xy}\sigma_y) \tag{8.9a}$$

$$\varepsilon_y = \frac{1}{E}(\sigma_y - \nu_{yx}\sigma_x) \tag{8.9b}$$

$$0 = \frac{1}{E}(-\nu_{zx}\sigma_x - \nu_{zy}\sigma_y) \tag{8.9c}$$

The first two equations are identical to the equations of plane stress, which can be rearranged such that:

$$\begin{bmatrix}\sigma_x \\ \sigma_y\end{bmatrix} = \frac{E}{1-\nu^2}\begin{bmatrix}1 & \nu_{xy} \\ \nu_{yx} & 1\end{bmatrix}\begin{bmatrix}\varepsilon_x \\ \varepsilon_y\end{bmatrix} \tag{8.10}$$

The final equation above seems to imply that $\sigma_x = -\sigma_y$, which does not seem reasonable (e.g., stretching in one direction does not cause graphene or similar 2D material to undergo equivalent compression in the other direction). However, we realize that both Poisson ratios are in terms of the component "z." Since $\nu_{ij} = -\varepsilon_i/\varepsilon_j$ where $\varepsilon_z = 0$, then $\nu_{zx} = \nu_{zy} = 0$, and

$$0 = \frac{1}{E}(-\nu_{zx}\sigma_x - \nu_{zy}\sigma_y) = \frac{1}{E}(-(0)\sigma_x - (0)\sigma_y) \tag{8.11}$$

So 2D materials can be represented by classical plane stress conditions while neglecting and strain in the third direction. Introducing shear contributions and assuming, in plane, that $\nu_{xy} = \nu_{yx} = \nu$, results in

$$\begin{bmatrix}\sigma_x \\ \sigma_y \\ \tau_{xy}\end{bmatrix} = \frac{E}{1-\nu^2}\begin{bmatrix}1 & \nu & 0 \\ \nu & 1 & 0 \\ 0 & 0 & \frac{1}{2}(1-\nu)\end{bmatrix}\begin{bmatrix}\varepsilon_x \\ \varepsilon_y \\ \gamma_{xy}\end{bmatrix} \tag{8.12}$$

While it may be simple to state that 2D materials can be considered plane stress, it is critical to understand that the underlying assumptions are different – the resulting formulation is just a convenient interpretation.

With these formulations, multiaxial stress/strain conditions can be applied to extract a number of critical properties via the calculation of virial stress as discussed in Section 8.4.1. In terms of uniaxial strength (ultimate stress) or even biaxial strength (when $\sigma_x = \sigma_y$), the maximum value is taken from the test simulation.

8.4.3 Stiffness

Beyond strength, planar stiffness or axial rigidity is a key mechanical property of 2D materials. Quite different approaches have been employed to derive and measure the stiffness of 2D materials [16]. From a 3D continuum mechanics approach, the stiffness coefficients are defined by

$$C_{ijkl} = \frac{\partial^2 u}{\partial\varepsilon_{ij}\partial\varepsilon_{kl}} \tag{8.13}$$

where u is the potential energy density of the system, and ε_{ij} and ε_{kl} are strains along different orientations. Again, for details, the reader is directed to any classical elasticity text. We note

the relationship with Eq. (8.1) resulting in

$$C_{ijkl} = \frac{\partial}{\partial \varepsilon_{kl}} \sigma_{ij} \tag{8.14}$$

which leads to the colloquial (but useful) definition that the stiffness coefficients are simply the derivative of the stress–strain relation. For uniaxial conditions, as described earlier, the Young's modulus (E) can be defined as

$$E = C_{xxxx} = \frac{\partial^2 u}{\partial {\varepsilon_{xx}}^2} = \frac{\partial^2 u}{\partial {\varepsilon_x}^2} \tag{8.15}$$

where again u is the strain energy density and ε_x the strain in the uniaxial direction. Note that, in Eq. (8.15), there is no need to calculate any stress quantities – merely the total strain energy. This is beneficial in energetic or *ab initio* approaches, such as the aforementioned DFT approach, which does neither applies potentials nor derives forces, negating the virial stress.

Typically, the strain energy density u is defined as the total energy U per volume V, or $u = U/V$. For 2D materials, however, the strain energy can be defined per unit area, as there is no definitive "thickness." As such, the 2D modulus can be defined as

$$E_{2D} = \frac{1}{A_0} \frac{\partial^2 U(\varepsilon)}{\partial {\varepsilon_2}^2} \tag{8.16}$$

where U is the total energy of a 2D system of finite area A_0. The ambiguity for the thickness of monoatomic crystal structures such as graphene and other 2D nanomaterials has been discussed in a previous study [54], and due to the buckled structure of some 2D nanomaterials such as silicene, it is difficult to theoretically assign. This situation has been discussed in previous studies [16], suggesting the stress and elastic moduli of monolayer systems be reported in force per unit length (N/m) rather than force per unit area (N/m^2 or Pa), consistent with Eq. (8.15). As such, the in-plane stiffness and in-plane stress (maximum force per unit length) are more accurately used to represent the stiffness and strength of the structure, for a more apt comparison to other 2D crystals where σ and ε are the stress and strain [54, 55]. Note that the 2D modulus can be derived for any thin 2D-like system, by scaling the traditional modulus by the height of the system, or $E_{2D} = Eh$.

Since, if using MD approaches, stress can be calculated, we can alternatively use the stress–strain relation to determine uniaxial moduli. The modulus/stiffness can be then calculated by

$$E = \frac{\partial \sigma_x}{\partial \varepsilon_x} \tag{8.17}$$

where σ_x and ε_x are the stress and strain, and the subscript "x" indicates the direction of loading. Thus, a tangential fitting of the stress–strain response of a 2D material will indicate the stiffness at a particular strain value. A linear fit of the initial small deformation regime is typically associated with the Young's modulus E.

A careful scrutiny between Eqs (8.14) and (8.17) indicates that they may not result in the same quantity. If using viral stress, the definition of σ_x only considers components of force in the x-direction, thus energetic components in other directions may be omitted from the calculation. Coupling of deformation mechanisms may increase or decrease the strain energy density, u, without emerging in the σ_x calculation. Thus, both approaches are necessary to reveal any atomistic mechanisms that may not be apparent *a priori* when calculating stiffness.

Following the simple derivation of Young's modulus as indicated by Eq. (8.17), other classical mechanical properties such as the shear modulus and bulk modulus can be calculated in a similar manner. We first consider Hooke's law in shear:

$$\tau = G\gamma \tag{8.18}$$

where the shear stress τ is related to the shear strain γ via the shear modulus G. The continuum interpretation of the shear modulus can be stated as

$$G = C_{xyxy} = \frac{\partial^2 u}{\partial \varepsilon_{xy}{}^2} = \frac{\partial}{\partial \varepsilon_{xy}}\sigma_{xy} = \frac{\partial \tau_{xy}}{\partial \gamma_{xy}} \tag{8.19}$$

where $\sigma_{xy} = \tau_{xy}$. Subjecting a system to simple shear strain, γ_{xy}, we can again use tangential or linear fits to attained data to derive a shear modulus. Of note, subjecting shear to 2D system commonly results in out-of-plane buckling due to the compressive response, limiting the applied shear strain range. In effect, the shear stiffness is relatively easy to determine in the small deformation regime, but the shear strength is more difficult to achieve due to nonlinear geometric effects.

Finally, the bulk modulus can be determined via a biaxial straining of a 2D system. While bulk modulus K typically relates hydrostatic stress to volumetric change for 2D systems, the equivalent K_{2D} related biaxial stress to areal change defined by

$$\sigma_{\text{biaxial}} = K_{2D}\frac{\Delta A}{A_0} \tag{8.20}$$

where ΔA is the change in area, A_0 the initial area, and σ_{biaxial} is the stress simultaneously applied in the x- and y-directions.

8.4.4 Effect of Bond Density

The remarkable strength and stiffness are commonly considered a function of their limited "thickness," as all chemical bonds are limited in-plane, and thus appear "stronger" in that direction. Thus, the strength is merely a result of a higher, planar bond density due to 2D structures. This idea can be explored if one could vary the bond density of a structure, while the geometry remains the same. Theoretically, this is possible in extended graphynes.

We have established that the strain energy and deformation of graphene or silicene sheets can be described by continuum elasticity theory [56–58], and as such the same assumptions are applied to graphynes. Likewise, for the mechanical characterization, it is assumed that under small deformation, graphyne can be approximated as a linear elastic material. Previous studies have reported a continuous degradation of modulus with the introduction of acetylene links (n) from graphyne ($n = 1$) to graphtetrayne ($n = 4$). The relatively smooth degradation as a function of bond density through n can be extended and predicted via a simple spring model formulation. The springs model can be used to predict the mechanical properties of graphynes with arbitrarily long acetylenic linkages, considering the graphyne system as a network of springs (see Figure 8.3). Such an elastic approximation (similar to a truss model) has been introduced for graphene [59] and carbon nanotubes [60]. The stiffness of a single segment can be written as

$$K = \left[\frac{1}{k_0} + \frac{n}{k}\right]^{-1} \tag{8.21}$$

where k_0 is the stiffness of the aromatic group and k is the stiffness of a single acetylene link. If we presume that $k_0 \gg$ k (e.g., deformation occurs predominately in the link, supported by previous MD results [61, 62], then ${k_0}^{-1} \rightarrow 0$, such that

$$K \cong \left[\frac{n}{k}\right]^{-1} \cong \frac{k}{n} \tag{8.22}$$

We associate this linear spring stiffness to an effective modulus, where $K = EA_0/L$ (for the 2D perspective, EA_0 can be replaced with $E_{2D}b$, where b is the planar width of the system). The force required for unit strain can be written as

$$KL = EA_0 \tag{8.23}$$

We assume that strain predominately occurs along the acetylenic links (due to $k_0 \gg k$; see Figure 8.3(a), such that $L = L_n = nL_0$, where L_0 is the summed distance of a carbon–carbon single and carbon–carbon triple bond. Thus,

$$KL = KL_n = KnL_0 = kL_0 = \text{constant} \tag{8.24}$$

Thus, similar to adding equivalent springs in series, the material behavior is deemed constant, regardless of the number of acetylene links. The effective area per spring, however, changes as a function of n. The associated cross-sectional area per link can be represented by ${A_n}^{\text{cross}} = l_n t$, where t is the effective thickness of the graphyne plane (taken as the van der Waals spacing, $t = 3.2$ Å) and l_n the equivalent length of the weighted area, and $l_n \propto a$, the lattice spacing (see Figure 8.10(a) and (b)). From Eqs (8.23) and (8.24), it follows that $Y_n {A_n}^{\text{cross}} =$ constant, and thus

$$E_n = E_1 \left(\frac{a_1}{a_n}\right) \tag{8.25}$$

In general, $E_n \propto C{a_n}^{-1}$, where the constant here is fitted by the parameters of graphyne ($n = 1$), for example, $C = Y_1 a_1$. The simple spring formulation can be used to predict the elastic modulus of arbitrary graph-n-yne and shows that the stiffness decreases as the bond density (through n) decreases.

8.4.5 Bending Rigidity

Theoretical studies and synthesis [63, 64] have suggested that bending stiffness of monolayer graphene is critical in attaining the structural stability and morphology of graphene sheets, which in turn could have important impacts on their electronic properties. This would similarly hold for other 2D crystal structures such as silicene. Due to the relative flexibility and single atom thickness of 2D monolayer materials, a mechanical bending test is difficult to implement. It is very difficult to apply a bending moment directly to such structures as local bending on a membrane structure would induce local curvature only. To circumvent this issue, the isotropic bending modulus is determined by 1D pure bending experiments using molecular statics in which curvature is induced (and fixed) prior to energy minimization, similar to previous coarse-grain [65] and full atomistic [7, 57, 66] investigations. To calculate the bending modulus of 2D monolayer materials, a rectangular sheet is bent into a section of a cylinder with constant radius of curvature throughout the basal plane (Figure 8.11(b)). The neutral

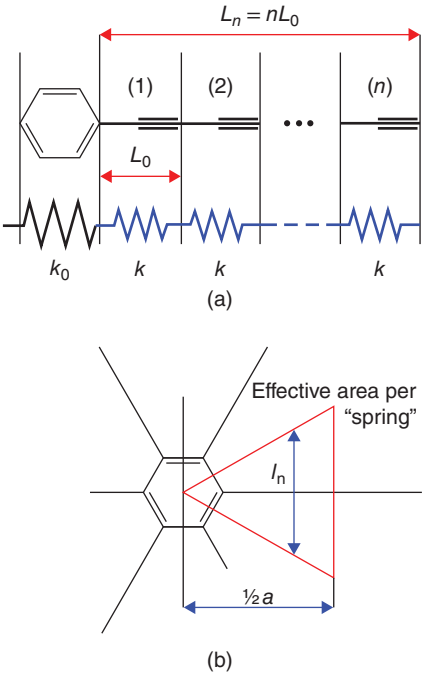

Figure 8.10 Simple spring–network model representation for scaling law. (a) Serial spring representation for the acetylene links. (b) The linear spring stiffness can be associated to an effective modulus via an effective cross-sectional area

plane for pure bending is parallel to the layer and passes through the centroid of the bending cross section.

The edges of the bent sheet are kept fixed and the bulk of the sheet is allowed to relax subject via low-temperature equilibrium and energy minimization. To avoid boundary effects at the fixed edges, the elastic energy is only considered for the interior portion of the sheet. At finite temperatures, graphene, graphyne, and silicene exhibit ripples and undulations out-of-plane (Figure 8.11(a)). As such, the material structure deviates from the ideal curvature initially imposed and the derived stiffness can be considered the effective bending modulus. However, both the low-temperature equilibrium and minimization process limit the observed ripples, and the system curvature is maintained.

The bending modulus is obtained by curve fitting with energy versus curvature data points, using the following expression for elastic bending energy

$$U = \frac{1}{2} D\kappa^2 \tag{8.26}$$

where U is the system strain energy per unit basal plane area (eV/nm^2), D is the bending modulus per unit width (eV), and κ is the prescribed beam curvature. A range of curvature is imposed on the system and the minimized energies are plotted versus κ (Figure 8.11(c)).

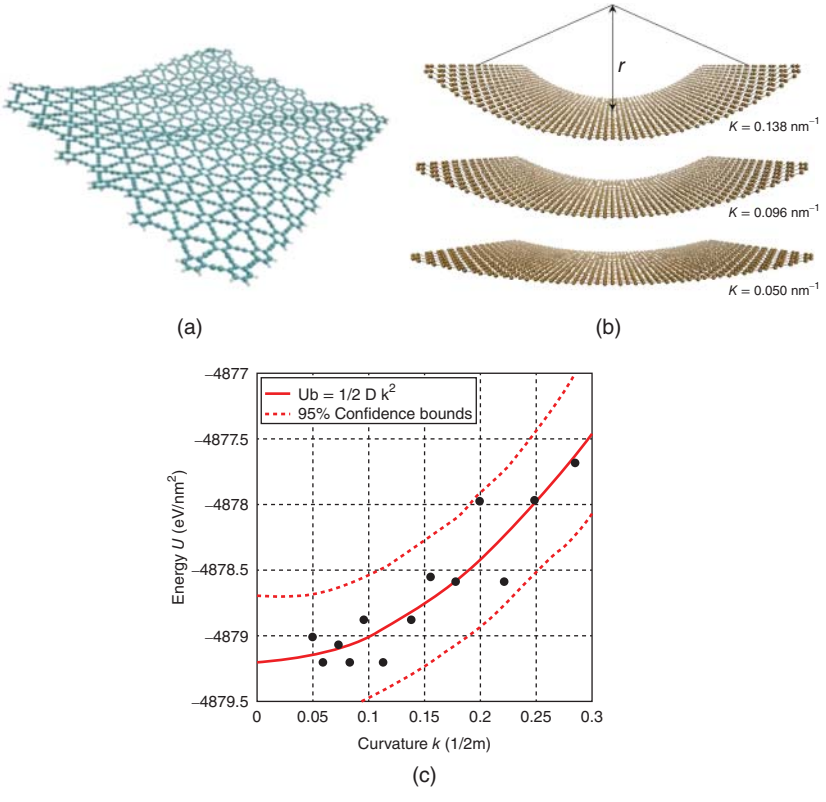

Figure 8.11 (a) Stable graphyne structure after minimization and equilibration of 0.5 ns at a temperature of 300 K. (b) Schematic illustration of a 2D silicene sheet bended with an imposed radius of curvature $\kappa = 1/r$. (c) Energy versus curvature for a silicene sheet with 95% confidence bounds

We note that the bending rigidity, D, is equivalent in function to the bending rigidity of a classical beam, EI, where E is the Young's modulus of the material and I is the second area moment of inertia. The inertia is involved due to the assumption that (1) a neutral axis exists in the cross section of the beam and (2) the section is in both tension and compression, changing once crossing the neutral axis. This core assumption, however, is meaningless for monoatomistically thin structures – is a single carbon atom, once bent in a graphene sheet, in compression or tension? The question is moot. The resistance to bending does not come from inertia effects, but rather due to electron orbital deformation and overlap. This, in turn, causes an energy increase and bending "rigidity." However, for multilayer systems (bilayer and greater), it has been shown that the bending modulus is proportional to the cube of the height of the cross section ($D \propto Eh^3$), in agreement with continuum interpretations [7, 65]. Indeed, once the system has "thickness," a neutral axis can be assumed and atoms can be in compression or tension accordingly. Note that this interpretation does not change the definition or utilization of D in the above-mentioned equation.

8.4.6 Adhesion

Due to the relatively high ratio of surface area to mass (e.g., specific surface area) and the propensity for surface interaction, the resulting adhesion plays an important role in many important technological applications of 2D materials. Graphene and other 2D materials, structures, and devices are increasingly influenced by surface forces due to the weak vdW interactions, especially as their size moves into the nanometer range. This occurs because the materials are often separated by small (interlayer) distances and are sensitive to the operant range of surface forces, and the structural stiffness decreases as its size decreases. For example, adhesive interactions are critical to nanomechanical devices [67] such as graphene switches – actuated electrostatically to bring them into, or near, contact with an electrode, while van der Waals forces can permit the release of the switch [68, 69]. Whether 2D materials are a promising nanoelectronics material depends predominantly on the nanostructure's mechanical integrity and ability to integrate or to adhere to electronic substrates.

Moreover, one of the most utilized fabrication methods of 2D materials involves CVD growth on an appropriate substrate followed by batch transferring it from the host substrate to a functional target material for device applications [70]. Another widely used technique for exfoliation of few- and mono-layered graphene is based on tearing-off graphene layers using adhesive tape [1, 71]. In both cases, the understanding of adhesion to both substrate and target material plays a crucial role in this process. The engineering of the peeling, stamping, and other fabrication processes also depends on the adhesion of the 2D layers. There is, therefore, an urgent need for experimental methods to characterize the mechanical properties and adhesion behavior.

It is well demonstrated that adhesion energies for different crystallographic stacking configurations for 2D materials such as graphene and BN show that the interlayer bonding and adhesion are due to the long-range van der Waals (vdW) forces [72]. In MD simulation, the vdW interaction is typically represented by a Lennard–Jones function – a mathematically simple model that approximates the interaction between a pair of neutral atoms and molecules. A Lennard–Jones 12:6 function is given as

$$\phi_{\mathrm{LJ}} = 4\varepsilon_{\mathrm{LJ}}\left[\left(\frac{\sigma_{\mathrm{LJ}}}{r}\right)^{12} - \left(\frac{\sigma_{\mathrm{LJ}}}{r}\right)^{6}\right] \tag{8.27}$$

where $\varepsilon_{\mathrm{LJ}}$ is the energetic depth of the potential well, σ_{LJ} is the finite distance at which the interparticle potential is zero, and r is the distance between the particles. The Lennard–Jones potential is a relatively good approximation to model dispersion and overlap interactions in molecular models. Applied to a system of 2D materials (e.g., a bilayer of two sheets), the interaction between the sheets at equilibrium is directly proportional to both the number of atoms, n, and the energy per atom, $\varepsilon_{\mathrm{LJ}}$. It follows that the adhesion energy will scale with the area A of the sheets (assuming that the areal atomistic density, $\rho_A = n/A$, is constant). Thus, one can conclude that the adhesion energy, U_{adhesion}, is proportional to both $\varepsilon_{\mathrm{LJ}}$ and A. Note that $U_{\mathrm{adhesion}} \neq n\varepsilon_{\mathrm{LJ}}$ due to the long-range multineighbor interaction of the vdW forces, but $U_{\mathrm{adhesion}} \propto \varepsilon_{\mathrm{LJ}}$.

Using DFT or MD methods, the adhesion energy can be easily determined by direct measurement or by fitting the energy landscape. Direct measurement simply quantifies the energy change, ΔU, between an adhered system and a detached system of two sheets, sheet with substrate, sheet with molecule, and so on. Two simulations are required – one in which the 2D

sheet is detached and beyond the interaction range of the vdW forces ($r \to \infty$), and the other in which the 2D sheet is adhered to the target at equilibrium ($r = r_0$). The energy change can be calculated by the simple difference of minimized system energies, where

$$U_{\text{adhesion}} = \Delta U = U(r \to \infty) - U(r = r_0) \tag{8.28}$$

If the area of 2D material is known, the adhesion energy can be calculated per area where

$$\gamma = \frac{U_{\text{adhesion}}}{A_0} \tag{8.29}$$

Beyond the simple strength of adhesion, the entire energy landscape during separation may be required to indicate the decay of interaction and shed light on phenomena such as electrostatic screening. Again, the simulation process is relatively trivial – instead of a two-point difference of energy, from $r = r_0$ to $r \to \infty$, the energy is tracked in discrete steps, such that $U_{\text{adhesion}} = f(r)$ can be plotted, for example, the energy landscape. Variations in separation procedure (e.g., shearing effects, introduction of nanoparticles) can explore different adhesion phenomena. Once the energy landscape is determined, statistical fitting methods can be used to describe the adhesion behavior. Energy can be scaled such that when $r \to \infty$, $U_{\text{adhesion}}(r) \to 0$, and in such a case:

$$\gamma = \frac{\min(U_{\text{adhesion}}(r))}{A_0} \tag{8.30}$$

Using simulation methods to determine adhesion strength is trivial, as the simulation interactions are formulated using potential energies and the values of any atom at any time can be extracted. This is not the case for experimental measures – there is no method to directly "measure" the potential energy of a single atom when adhered to a substrate. Rather, indirect measurements may be made exploiting the presumed elastic and adhesion behavior of a membrane-like system. Many ingenious methods have been derived by researchers in the field. Here, for brevity, we discuss two examples.

Zong et al. developed a technique to characterize adhesion of monolayered/multilayered graphene sheets on silicon wafer [73]. Nanoparticles trapped at graphene–silicon interface act as point wedges to support axisymmetric blisters (see Figure 8.12(a)–(c)). Local adhesion strength is found by measuring the particle height and blister radius using a scanning electron microscope. It was assumed that graphene behaved as a flexible membrane with negligible flexural rigidity. Using a continuum formulation, a governing equation was derived analogous to that of a thin membrane clamped at the periphery and being transversely loaded at the center [74]. At equilibrium, the blister contracts to a radius a and the adhesion energy can be calculated by

$$\gamma = Eh\left(\frac{w}{2a}\right)^4 \tag{8.31}$$

where E is the Young's modulus of the graphene, h the effective height of the multilayers (thus, "Eh" representing the 2D modulus as previously discussed), w the height of the blister, and a is the radius of the blister.

Alternatively, Lu and Dunn considered a 2D membrane that is adhered to a substrate over a cavity by van der Waals forces [75]. In the ground state (absence of an external load), the membrane adheres to the sidewalls over some distance, S, and is stretched flat between the walls over a distance L. This adhered length on the sidewall S and the tension in the membrane

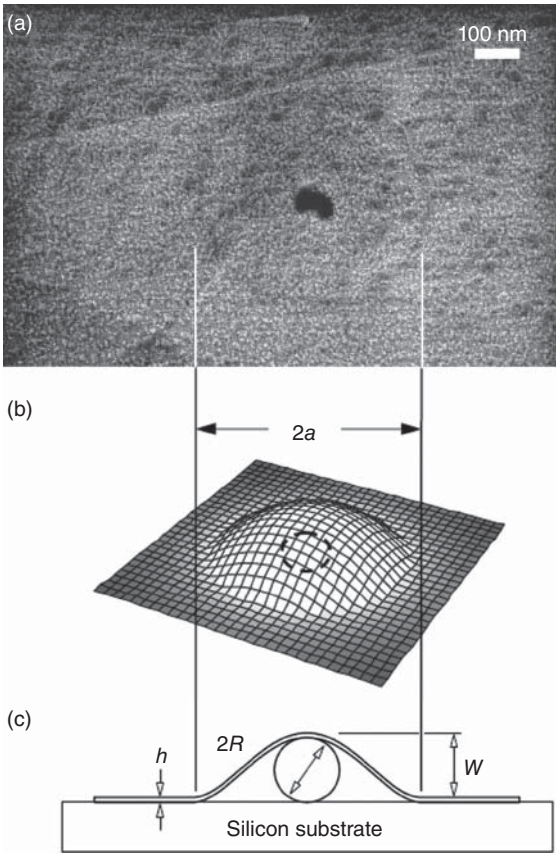

Figure 8.12 Nanoparticles trapped in a circular blister at graphene–silicon interface. (a) SEM image, where the trapped particles appear dark. (b) 3D representation. (c) Blister model sketch. [73]

are determined by the balance of surface energy due to the van der Waals forces on the sidewalls and elastic energy associated with membrane stretching. The potential energy of the system can be formulated [75], and minimizing the potential energy yields the equilibrium length:

$$S = \gamma \frac{L(1-\nu^2)}{2Eh} \tag{8.32}$$

again, Eh appearing as the 2D modulus, L is the width of the cavity, and ν is the Poisson's ratio. If the equilibrium length can be measured, the adhesion energy can be calculated. The critical assumptions in indirect experimental measurement of adhesion strength typically lie in the selection of a continuum approximation (e.g., membrane-like behavior for both the described approaches). Typically, such models are further validated against molecular simulation (if possible) to indicate any deviations due to atomistic phenomenal.

Adhesion is critical to the multilayered 2D structures (e.g., graphene–graphene), heterogeneous stacked layers (e.g., graphene–BN [76]), 2D materials on substrates (e.g., graphdiyne on copper), self-folded geometries (see Section 8.4.7), among others. Combined

with high flexibility, 2D materials behave as ultimate thin membranes, and with adhesion conform more closely to a surface than any other solid. This provides new opportunities to study solid–solid surface interactions including the effects of even the smoothest surface topographies and potentially the nature of van der Waals and Casimir forces. The interplay of elastic and adhesion energies is shown to lead to stacking disorder and moiré structures. The dispersion, absolute band gaps, and low-energy electronic states are also dependent on the resulting stacked/adhered structures [76], once again opening yet another potential design variable.

8.4.7 Self-Adhesion and Folding

One of the consequences of a propensity of 2D layers to adhere in a multilayer manner is that, upon folding, they may also self-adhere. Although planar sheets are the most common form of such materials, scrolled and folded morphologies have attracted great interest because of their potential properties [77]. Like a sticky piece of paper folded on itself, the relative flexibility of 2D materials opens up a new field of topological possibilities and the so-called nano- or meso-origami. Indeed, the folding of paper and fabrics has been used for millennia to achieve enhanced articulation, curvature, and visual appeal for intrinsically flat, 2D materials [78]. For 2D materials, folding may transform it to complex shapes with new and distinct properties, opening up an entirely new paradigm of material's design.

From a mechanical perspective, recent studies show that suspended graphene sheets can fold and form folded edges due to van der Waals (vdW) interaction [65, 79–81]. The folded edges of graphene sheets show racket shapes with structures similar to carbon nanotube walls (Figure 8.13(a)–(d)), which can have strong influence on the electronic and magnetic properties of graphene [82–84]. The folded racket-shape graphene consists of a curved region of length $2L$ and a flat region of length L_0. The total length of the folded system is thus $L_{\text{total}} = 2L + 2L_0$. Note the adhered layers still maintain an equilibrium interlayer distance, congruent with the associated vdW adhesion. Clearly, the configuration of the folded graphene sheet results from the competition between adhesion energy U_{adhesion} in the flat region and bending energy U_{bending} in the curved region. This is a key behavior that also dictates the minimal crease size in multiple folded [79, 85] or crumpled 2D materials [86–88]. If the flat graphene is considered as the ground state, the energy of the folded graphene sheet is simply:

$$U_{\text{total}} = U_{\text{bending}} + U_{\text{adhesion}} \tag{8.33}$$

The adhesion energy denotes the binding energy per unit area of graphene, and the bending energy is due to the necessary imposed curvature. The adhesion energy can be expressed as $U_{\text{adhesion}} = -\gamma L_0$ with γ denoting the binding energy per unit area of graphene (as per the previous section, $\gamma \propto \varepsilon_{\text{LJ}}$). In terms of the curved length:

$$U_{\text{total}}(L) = U_{\text{bending}} - \gamma \left(\frac{1}{2} L_{\text{total}} - L \right) \tag{8.34}$$

Two cases arise from this simple relation:

1. If the total length of graphene is too short, the total energy $U_{\text{total}} > 0$, the resistance from the curved region can overcome the adhesion from the flat region, and therefore the folded configuration is unstable and can unfold.

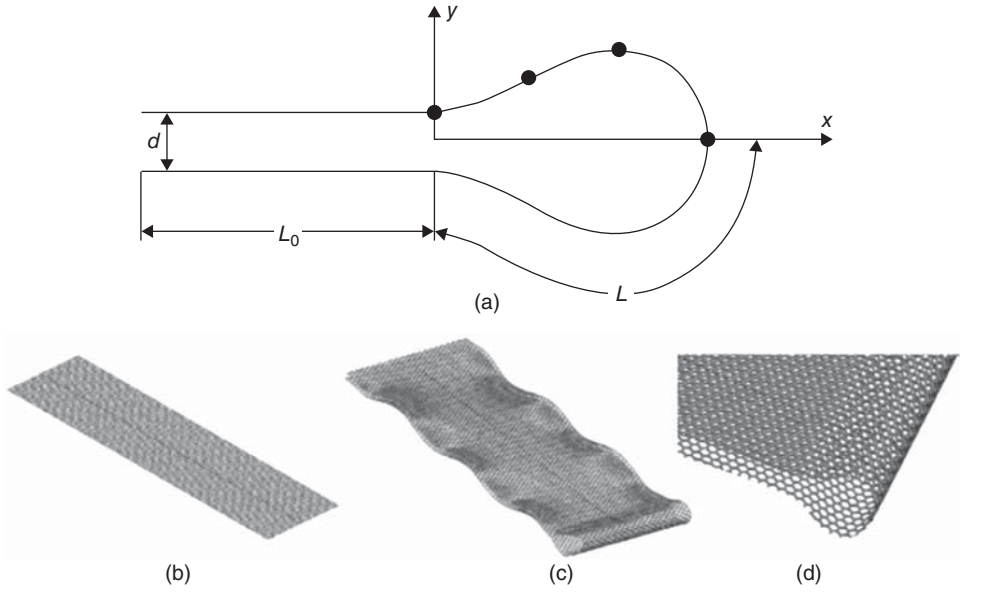

Figure 8.13 Folded configurations of graphene sheet. (a) Schematic of a folded single-layer graphene. (b) Flat state and (c) folded configuration of monolayer graphene from MD model. (d) Enlarged view of the folded graphene edge. [79, 85]

2. If the total length of graphene is long enough, the total energy $U_{\text{total}} < 0$, the adhesion energy over the flat region exceeds the resistance from the curved region, and therefore the folded graphene is energetically preferred and stable.

Obviously, there exists a critical length L_{critical} such that $U_{\text{total}} = 0$, which separates the stable and the unstable folded configurations of graphene.

A recent study by Cranford et al. [65] established a small deformation mechanics model to reveal the critical folding length of multilayered graphene sheets. Modeling the folded length of the graphene sheet as two symmetric linear elastic beams, the bending energy per unit length can be defined as

$$U_{\text{bending}} \cong 2D_{\text{multi}} \int_0^L \left(\frac{d^2u}{dx^2}\right)^2 dx \tag{8.35}$$

where D_{multi} is the bending stiffness of a multilayer system (per unit width) and $u(x)$ is the presumed beam deflection. Applying the Euler–Bernoulli beam equation to derive $u(x)$ with associated small deformation boundary conditions, the total energy of the system per unit width can be expressed as

$$U_{\text{total}}(L) = \frac{2\pi^2}{L} D_{\text{multi}} - \gamma\left(\frac{1}{2}L_{\text{total}} - L\right) \tag{8.36}$$

Through minimization of the above with respect to L, we find

$$L_{\text{critical}} = \pi\sqrt{\frac{2D_{\text{multi}}}{\gamma}} \tag{8.37}$$

While approximated with small deformation assumptions, the above relation was validated with simulations of single-layer graphene and multilayer systems (up to 10 layers) with little appreciable error [65]. As predicted by Eq. (8.37), the folded length of the graphene sheet is proportional to the square root of the bending stiffness. It is also noted that the total length of the graphene, L_{total}, must be such that a folded confirmation is energetically favorable (i.e., $|U_{\text{adhesion}}| > |U_{\text{bending}}|$), but does not affect the critical folded length (however, the total length does result in a change in the absolute value of the energy minima). However, predicted shapes of the folded graphene edges are not accurately described by the above formulation, partly because small deformation models cannot accurately predict the shapes of folded graphene edges. Meng et al. [79] developed a finite deformation theoretical model to study the folding of single-layer graphene, which can accurately predict not only the critical length of single-layer graphene folding but also the shape of the folded edge. In a follow-up study, Meng et al. [80] also explored multilayered graphene-folded structures, using a similar finite deformation beam theory approach. For both single- and multilayered racket shapes, the deformed geometry of the sheets can be completely described by two quantities, κ_0 and κ_1, defined by the Cartesian coordinates of the curved region of the middle plane under curvature (e.g., the neutral axis in classical beam theory). The bending energy in the racket-shaped curved region, U_{bending}, can be obtained by a first-order approximation as [79, 80]:

$$U_{\text{bending}} = 2D_{\text{multi}} \int_0^{\alpha} \sqrt{\kappa_0^2 - (\kappa_1^2 - \kappa_0^2)\sin\theta}\, d\theta + D_{\text{multi}} \int_0^{\frac{\pi}{2}} \sqrt{\kappa_0^2 + (\kappa_1^2 - \kappa_0^2)\sin\theta}\, d\theta \tag{8.38}$$

where D_{multi} is the bending stiffness of the multilayer graphene, $\alpha = \sin^{-1}(\kappa_0^2/\kappa_1^2 - \kappa_0^2)$, and the governing equations for κ_0 and κ_1 can be solved numerically [79], leading to the numerical solution for U_{bending}. The total energy of the folded/adhered graphene sheet is still equal to Eq. (8.38), with a more complex (and accurate) term substituted for U_{bending}. Minimization of the total energy can then give a precise solution to multilayer folding via numerical methods. For brevity, complete solution details can be found in the original works by Meng et al. [79, 80].

Beyond racket-type folding, other self-adhering and folding phenomena has been investigated in a similar mechanistic manner, including self-scrolling graphene [89, 90], nanoscrolls with carbon nanotubes [91, 92], graphene peeling [7, 93], surface crumpling [87], surface folding [94], and self-opening capsules [95, 96], to name a few. We note that the energy balance approach described here does not consider an external energy source, which can be used as control mechanisms. Indeed, mechanical stimulation can help initiate self-folding and overcome energy barriers [97] or, alternatively, trigger unfolding [77] depending on system stability. Also complicating matters depending on the direction or location of initial folding line formations, certain directions of folding, may be more energetically favorable than others [97, 98]. Exploiting the potential of folding 2D materials is still in its infancy. In principle, single or periodic hems, pleats, creases, ripples, and ruffles can be tailored from such planar sheets. Critical to such applications is the mechanistic understanding of folding, stability, and limit states, as outlined earlier.

8.5 Failure

In addition to stiffness and strength, of utmost importance for 2D materials is how they fail. Characterized by repeating crystalline structures, such materials are typically prone to

lattice defects of various types (e.g., vacancies, Stone–Wales defects) and the associated stress concentrations when subjected to load. Thus, failure is typically characterized by local fracturing and dependent on the concentration of defects – a probabilistic metric. As such, we apply the mechanical tools of fracture analysis and failure statistics to 2D materials.

Here, in this section, the failure of 2D sheets, multilayers, or related composites with 2D crystallinity in the extreme condition is addressed based on the recent theoretical deterministic or statistical approaches of (1) quantized fracture mechanics (QFM) and (2) nanoscale Weibull statistics (NWS) proposed by Pugno and collaborators [99–101] and already extensively compared with experiments and atomistic simulations (also at the nanoscale). The role of thermodynamically unavoidable atomistic defects with different size and shape is thus quantified on brittle fracture and fatigue and even elasticity.

8.5.1 Quantized Fracture Mechanics

QFM is a reformulation of classical linear fracture mechanics with an explicit treatment of the discrete nature of atomistic bonds and crystallinity, and thus a "quantized" limit of crack growth and propagation. The reader is referred to the original works of Pugno and Ruoff for the complete formulations [101]. By considering QFM, the failure stress σ_N for a 2D material having "atomic size" q (the so-called "fracture quantum") and containing an elliptical hole of half-axes a perpendicular to the applied load and b parallel can be determined including in the asymptotic solution [101] the contribution of the far-field stress. We accordingly derived

$$\frac{\sigma_N(a,b)}{\sigma_N^{(\text{theo})}} = \sqrt{\frac{1+2a/q(1+2a/b)^{-2}}{1+2a/q}} \tag{8.39a}$$

where

$$\sigma_N^{(\text{theo})} = \frac{K_{\text{IC}}}{\sqrt{q\pi/2}} \tag{8.39b}$$

where $\sigma_N^{(\text{theo})}$ is the theoretical (defect-free) material strength (e.g., ~100 GPa for carbon nanotubes or graphene) and K_{IC} is the material fracture toughness. The self-interaction between the defect tips has been neglected here (i.e., $a \ll W$, with W the effective layer width of the 2D sheet) and would further reduce the failure stress. For atomistic defects (having characteristic length of few angstrom) in nanostructures (having characteristic size of several nanometers), this hypothesis is fully verified. However, QFM can also easily treat the self-tip interaction starting from the corresponding value of the stress-intensity factor (reported in the related Fracture Handbooks). The validity of QFM has been recently confirmed by atomistic simulations [99–102], and also at larger size scales [99, 100, 103], and for fatigue crack growth [100, 104, 105].

Regarding the defect shape, for a sharp crack perpendicular to the applied load $a/q =$ const & $b/q \to 0$, then $\sigma_N \approx \sigma_N^{(\text{theo})}/\sqrt{1+2a/q}$ and for $a/q >> 1$, that is, large cracks, $\sigma_N \approx K_{IC}/\sqrt{\pi a}$ in agreement with linear elastic fracture mechanics (LEFM). We note that LEFM can (1) only treat sharp cracks, and (2) unreasonably predict an infinite defect-free strength. On the other hand, for a crack parallel to the applied load $b/q =$ const and $a/q \to 0$, and thus $\sigma_N = \sigma_N^{(\text{theo})}$, as it must be. In addition, regarding the defect size, for self-similar and small

holes $a/b = \text{const}$ and $a/q \to 0$ and coherently $\sigma_N = \sigma_N^{(\text{theo})}$; furthermore, for self-similar and large holes $a/b = \text{const}$ and $a/q \to \infty$, and we deduce $\sigma_N \approx \sigma_N^{(\text{theo})}/(1 + 2a/b)$ in agreement with the stress concentration posed by elasticity; but elasticity (coupled with a maximum stress criterion) unreasonably predicts (3) a strength independent of the hole size and (4) tending to zero for cracks. Note the extreme consistency of Eq. (8.39) – that removing all the limitations of LEFM – represents the first law capable of describing in a unified manner all the size and shape effects for the elliptical holes, including cracks as limit case. In other words, Eq. (8.39) shows that the two classical strength predictions based on stress intensifications (LEFM) or stress concentrations (elasticity) are only reasonable for "large" defects; Eq. (8.39) unifies their results and extends its validity to "small" defects ("large" and "small" are here with respect to the fracture quantum). Finally, Eq. (8.39) shows that even a small defect can dramatically reduce the mechanical strength.

For multilayered composites, imposing the critical force equilibrium (mean-field approach), having different layers in numerical fractions f_{abN} containing holes of half-axes a and b for each material type N, we find the bundle/composite strength σ_C (ideal if $\sigma_C^{(\text{theo})}$) in the following form:

$$\frac{\sigma_C}{\sigma_C^{(\text{theo})}} = \sum_{a,b,N} f_{abN} \frac{\sigma_N(a,b)}{\sigma_N^{(\text{theo})}} \tag{8.40}$$

The summation is extended to all the different holes and material types; the numerical fraction f_{00N} is that of defect-free material N and $\sum_{a,b,N} f_{abN} = 1$. If all the defective layers are of the same material and contain identical holes $f_{abN} = f = 1 - f_{00N}$, and the following simple relation between the strength reductions holds:

$$1 - \sigma_C/\sigma_C^{(\text{theo})} = f\left(1 - \sigma_N/\sigma_N^{(\text{theo})}\right) \tag{8.41}$$

The previous equations are based on linear elasticity, that is, on a linear relationship $\sigma \propto \varepsilon$ between stress σ and strain ε. In contrast, let us assume $\sigma \propto \varepsilon^\kappa$, where $\kappa > 1$ denotes hyperelasticity, as well as $\kappa < 1$ elastic–plasticity. The power of the stress-singularity will accordingly be modified [106] from the classical value 1/2 to $\alpha = \kappa/(\kappa + 1)$. Thus, the problem is mathematically equivalent to that of a re-entrant corner [107], and consequently we predict

$$\frac{\sigma_N(a,b,\alpha)}{\sigma_N^{(\text{theo})}} = \left(\frac{\sigma_N(a,b)}{\sigma_N^{(\text{theo})}}\right)^{2\alpha} \tag{8.42}$$

A crack with a self-similar roughness, mathematically described by a fractal with noninteger dimension $1 < D < 2$, would similarly modify the stress-singularity, according to [108] $\alpha = (2 - D)/2$; thus, with Eq. (8.42), we can also estimate the role of the crack roughness. Both plasticity and roughness reduce the severity of the defect, whereas hyperelasticity enlarges its effect. For example, for a crack composed by n adjacent vacancies, we find $\sigma_N/\sigma_N^{(\text{theo})} \approx (1 + n)^{-\alpha}$.

According to LEFM and assuming the classical hypothesis of self-similarity ($a_{\max} \propto L$), that is, the largest crack size is proportional to the characteristic structural size L, we expect a size effect on the strength in the form of the power law $\sigma_C \propto L^{-\alpha}$. For linear elastic materials $\alpha = 1/2$ as classically considered, but for elastic–plastic materials or fractal cracks $0 \le \alpha \le$

$1/2$, whereas for hyperelastic materials $1/2 \leq \alpha \leq 1$, suggesting an unusual and superstrong size effect.

Equations (8.39)–(8.42) do not consider the defect–boundary interaction. The finite width $2W$ can be treated by applying QFM starting from the related expression of the stress-intensity factor (reported in relevant Handbooks). However, to have an idea of the defect–boundary interaction, we applied an approximated method, deriving the following correction $\sigma_N(a,b,W) \approx C(W)\sigma_N(a,b)$, $C(W) \approx (1-a/W)/(\sigma_N(a,b)|_{q\to W-a}/\sigma_N^{(\text{theo})})$ (note that such a correction is valid also for $W \approx a$, whereas for $W >> a$ it becomes $C(W >> a) \approx 1 - a/W$). Similarly, the role of the defect orientation β could be treated by QFM considering the related stress-intensity factor; roughly, one could use the self-consistent approximation $\sigma_N(a,b,\beta) \approx \sigma_N(a,b)\cos^2\beta + \sigma_N(b,a)\sin^2\beta$.

By integrating the quantized Paris' law, that is, an extension of the classical Paris' law recently proposed especially for nanostructure or nanomaterial applications [100, 104, 105], we derive the following number of cycles to failure (or life time):

$$\frac{C_N(a)}{C_N^{(\text{theo})}} = \frac{(1+q/W)^{1-m/2} - (a/W+q/W)^{1-m/2}}{(1+q/W)^{1-m/2} - (q/W)^{1-m/2}}, m \neq 2 \tag{8.43a}$$

and

$$\frac{C_N(a)}{C_N^{(\text{theo})}} = \frac{\ln\{(1+q/W)/(a/W+q/W)\}}{\ln\{(1+q/W)/(q/W)\}}, m = 2 \tag{8.43b}$$

where $m>0$ is the material Paris' exponent. Note that according to Wöhler $C_N^{(\text{theo})} = K\Delta\sigma^{-k}$, where K and k are material constants and $\Delta\sigma$ is the amplitude of the stress range during the oscillations.

Even if fatigue experiments in 2D materials are still to be performed, their behavior is expected to be intermediate between those of Wöhler and Paris, as displayed by all the known materials, and the quantized Paris' law basically represents their asymptotic matching (as QFM basically represents the asymptotic matching between the strength and toughness approaches). Only defects remaining self-similar during fatigue growth have to be considered, thus only a crack (of half-length a) is of interest in this context. By means of Eq. (8.43) the time to failure reduction can be estimated, similar to the brittle fracture treated by Eq. (8.39).

For a bundle or multilayered composite, considering a mean-field approach (similar to Eq. 8.40) yields

$$\frac{C_C}{C_C^{(\text{theo})}} = \sum_{a,N} f_{aN} \frac{C_N(a)}{C_N^{(\text{theo})}} \tag{8.44}$$

Better predictions could be derived integrating the quantized Paris' law for a finite width strip. However, we note that the role of the finite width is already included in Eq. (8.44), even if these are rigorously valid in the limit of W tending to infinity.

Regarding elasticity, interpreting the incremental compliance, due to the presence of the crack, as a Young's modulus (here denoted by E) degradation, we find $\frac{E(a)}{E^{(\text{theo})}} = 1 - 2\pi\frac{a^2}{A}$ [109]. Thus, recursively, considering Q cracks having sizes a_i or, equivalently, M different cracks with multiplicity Q_i ($Q = \sum_{i=1}^{M} Q_i$), noting that $n_i = \frac{2a_i}{q}$ represents the number of adjacent

vacancies in a crack of half-length a_i, with q atomic size, and $v_i = \frac{Q_i n_i}{A/q^2}$ its related numerical (or volumetric) vacancy fraction, we find [109]:

$$\frac{E}{E^{(\text{theo})}} = \prod_{i=1}^{Q} \frac{E(a_i)}{E^{(\text{theo})}} \approx 1 - \xi \sum_{i=1}^{M} v_i n_i \tag{8.45}$$

with $\xi \geq \pi/2$, where the equality holds for isolated cracks. Equation (8.45) can be applied to 2D materials and the related bundles or composites containing defects in volumetric percentage v_i.

Forcing the interpretation of our formalism, we note that $n_i = 1$ would describe a single vacancy, that is, a small hole. Thus, as a first approximation, different defect geometries from cracks to circular holes, for example, elliptical holes, could in principle be treated by Eq. (8.45); we have to interpret n_i as the ratio between the transversal and longitudinal (parallel to the load) defect sizes ($n_i = a_i/b_i$). Introducing the ith defect eccentricity e_i as the ratio between the lengths of the longer and shorter axes, as a first approximation $n_i(\beta_i) \approx e_i \cos^2\beta_i + 1/e_i \sin^2\beta_i$, where β_i is the defect orientation. For a single-defect typology $\frac{E}{E^{(\text{theo})}} \approx 1 - \xi v n$, in contrast to the common assumption $\frac{E}{E^{(\text{theo})}} \approx 1 - v$, rigorously valid only for the density, for which $\frac{\rho_C}{\rho_C^{(\text{theo})}} \equiv 1 - v$. Note that the failure strain for a defective 2D materials or related bundle can also be predicted by $\varepsilon_{N,C}/\varepsilon_{N,C}^{(\text{theo})} = (\sigma_{N,C}/\sigma_{N,C}^{(\text{theo})})/(E/E^{(\text{theo})})$. In contrast to what happens for the strength, large defectiveness is required to have a considerable elastic degradation, even if we have shown that sharp transversal defects could have a role.

8.5.2 *Nanoscale Weibull Statistics*

The discussed tremendous defect sensitivity, described by Eq. (8.39), is confirmed by a statistical analysis based on NWS [110], applied to the nanotensile tests. According to this treatment, the probability of failure P for a nearly defect-free structure under a tensile stress σ_N is independent of its volume (or surface), in contrast to classical Weibull statistics, namely:

$$P = 1 - \exp -N_N \left(\frac{\sigma_N}{\sigma_0}\right)^w \tag{8.46}$$

where w is the nanoscale Weibull modulus, σ_0 is the nominal failure stress (i.e., corresponding to a probability of failure of 63%), and $N_N \equiv 1$. In classical Weibull statistics $N_N \equiv V/V_0$ for volume-dominating defects (or $N_N = A/A_0$ for surface-dominating defects), that is, N_N is the ratio between the volume (or surface) of the structure and a reference volume (or surface).

Moreover, defects are thermodynamically unavoidable, especially at the large size scale. At the thermal equilibrium, the vacancy fraction $f = n/N << 1$ (n is the number of vacancies and N is the total number of atoms) can be estimated as

$$f \approx e^{-E_1/k_B T_a} \tag{8.47}$$

where E_1 is on the order of a few eV, the energy required to remove one atom of the system to create the vacancy and T_a is the absolute temperature at which the material is assembled

(e.g., for carbon $E_1 \approx 7$eV and T_a typically in the range between 2000 and 4000 K, thus $f \approx 2.4 \times 10^{-18} - 1.6 \times 10^{-9}$). The strength of the structure will be dictated by the largest transversal crack on it, according to the weakest link concept. The probability of finding a nanocrack of size m in a bundle with vacancy fraction f is $P(m) = (1-f)f^m$, and thus the number M of such nanocracks in a bundle or composite composed by N atoms is $M(m) = P(m)N$. The size of the largest nanocrack, which typically occurs once, is found from the solution to the equation $M(m) \approx 1$, which implies [111]:

$$m \approx -\ln[(1-f)N]/\ln f \approx -\ln N/\ln f \tag{8.48}$$

Inserting Eqs (8.47) and (8.48) into Eq. (8.39) evaluated for a transversal crack ($b \approx 0$ and $2a/q \approx m$), we deduce the statistical counterpart of Eq. (8.39) and thus the following thermodynamical maximum achievable strength:

$$\frac{\sigma_N(N)}{\sigma_N^{(\text{theo})}} \leq \frac{\sigma_N^{(\max)}(N)}{\sigma_N^{(\text{theo})}} = \frac{1}{\sqrt{1 + \frac{k_B T_a}{E_1} \ln N}} \tag{8.49}$$

The fracture mechanics approach could be of interest to evaluate the strength or assuming a different failure mechanism, not intrinsic fracture as previously treated but rather as a sliding failure mode [112]. Thus, we assume the interactions between adjacent layers as the weakest links, that is, the fracture of the bundle or composites is caused by layers sliding rather than by their intrinsic fracture.

Accordingly, the energy balance during a longitudinal delamination (here "delamination" has the meaning of Mode II crack propagation at the interface between adjacent nanotubes) dz under the applied force F is

$$d\Phi - Fdu - 2\gamma(P_C + P_{vdW})dz = 0 \tag{8.50}$$

where $d\Phi$ and du are the strain energy and elastic displacement variation due to the infinitesimal increment in the compliance caused by the delamination dz; P_{vdw} describes the still existing van der Waals attraction (e.g., attractive part of the Lennard–Jones potential) for vanishing nominal contact perimeter (e.g., the shear force between two graphite single layers becomes zero for nominally negative contact area); γ is the surface energy of the layer–layer or layer–matrix interactions in bundles or composites. Elasticity poses $\frac{d\Phi}{dz} = -\frac{F^2}{2ES}$, where S is the cross-sectional surface area of the layers, whereas according to Clapeyron's theorem $Fdu = 2d\Phi$. Thus, the following simple expression for the bundle or composite strength ($\sigma_C = F_C/S$, effective stress and cross-sectional surface area are considered here; F_C is the force at fracture) is predicted:

$$\sigma_C^{(\text{theo})} = 2\sqrt{E\gamma\frac{P}{S}} \tag{8.51}$$

in which it appears the ratio between the effective perimeter P in contact and the cross-sectional surface area of the layers. Equation (8.51) can also be considered valid for the entire bundle, since we are assuming here the same value P/S for all the layers in the bundle. Note that Eq. (8.51) is basically the asymptotic limit for sufficiently long overlapping length, that is, the length along with two adjacent layers is nominally in contact; for overlapping length smaller than a critical value the strength increases by increasing the overlapping length; for a single

atomic layer this overlapping length is of the order of 10 nm, [113] it is expected to be larger for layers in bundles or composites, for example, of the order of several millimeters, as confirmed experimentally. This critical length is $\ell_C \approx 6\sqrt{\frac{hES}{PG}}$ where h and G are the thickness and shear modulus of the interface. It suggests that increasing the size-scale $L \propto \sqrt{S} \propto P \propto h$ this critical length increases too, namely $\ell \propto L$, thus the strength increases by increasing the overlapping length in a wider range; however, note that the achievable strength is reduced since $\sigma_C^{(\text{theo})} \propto \sqrt{h\ell^{-1}} \propto \sqrt{P/S} \propto L^{-1/2}$, if $L \propto \ell \propto h$: increasing the overlapping length *ad infinitum* is not a way to indefinitely increase the strength. The real strength could be significantly smaller, not only because $\ell < \ell_C$ but also as a consequence of the misalignment of the layers with respect to the load axis. Assuming a nonperfect alignment of the layers in the bundle, described by a nonzero angle β, the longitudinal force carried by the layers will be $F/\cos\beta$; thus, the equivalent Young' modulus of the bundle or composites will be $E\cos^2\beta$, as can be evinced by the corresponding modification of the energy balance during delamination; accordingly

$$\sigma_C = 2\cos\beta\sqrt{E\gamma\frac{P}{S}} \tag{8.52}$$

For example, for graphene, the surface area for load transfer is doubled with respect to the case of the single carbon nanotube (the inner surface area does not contribute), the previous equation predicts for bundles or composites:

$$\sigma_C^{(\max,G)} = \sqrt{2}\sigma_C^{(\max,\text{CNT})} \tag{8.53}$$

For a comparison of QFM or NWS with experiments or simulations, see also [114–116].

8.6 Multilayers and Composites

Two-dimensional nanostructures such as graphene, hBN, and molybdenum disulfide (MoS_2) have attracted considerable attention because of their novel properties and versatile potential applications. These novel nanostructures have complementary physical properties. Therefore, 2D layers can be integrated into a multilayer stack to create 2D heterostructures that mitigate the negative properties of each individual constituent [117]. Layered crystals are characterized by strong intralayer covalent bonding and relatively weak interlayer van der Waals bonding. Since various methods have been proposed to make atomic layered 2D materials, such as graphene, hBN, TMDs, and oxides, it becomes possible to stack monolayers into variable configurations to build unique structures with desired functionalities [41].

Because of their equivalent structural parameters and distinct electronic properties, graphene and BN have been used in several studies to explore the possibility of making a graphene/BN composite. Several configurations of layered graphene/BN had been studied, such as graphene/BN to form a bilayer system [118], two or more BN layers [119], and 3D superlattice with alternate stacking of graphene and BN monolayers [120]. Other heterostructures such as monolayer [121] and bilayer [122] graphene sandwiched between two BN layers or monolayer BN sandwiched between two graphene layers [123] have also been constructed. Similarly, Jiang and Park [117] performed MD simulations to investigate the mechanical properties of single-layer MoS_2 and a graphene/MoS_2/graphene heterostructure under uniaxial tension. The results show that the Young's modulus of the heterostructure is about three times that of MoS_2. Although the stiffness is enhanced, the yield strain of the

heterostructure is considerably smaller than the MoS_2 due to lateral buckling of the outer graphene layers owing to the applied mechanical tension. Creating artificial heterostructures via stacking different 2D nanostructures on top of each other establishes a whole family of amazing materials with unusual characteristics and exciting possibilities for novel 2D devices [41].

Composite materials have advantages over traditional materials, where nanosized reinforcements are arranged in the matrix, presenting superior properties and added functionalities [2]. The excellent mechanical properties of 2D nanostructures, such as graphene, graphdiyne, and MoS_2, are promising reinforcements in high performance composites. The potential benefits of high strength and stiffness of 2D nanomaterial sheets in nanocomposites, combined with its low density compared with the density of metallic substrates, are easily recognized and are powerful incentives for the use of such materials in structural applications.

Metal–graphene nanolayered composites have been studied recently due to its promising applications (i.e., nuclear reactor structural material) and the effectiveness of graphene of significantly strengthening of metals. A reported study has demonstrated that the 2D geometry and low atomistic thickness of graphene can effectively constrain dislocation motion in polycrystalline metals, resulting in an engineered strengthening mechanism [124]. In a similar graphene/polymer composite (carbon monolayer + thin substrate), Gong et al. [125] demonstrated unambiguously that stress transfer takes place from the polymer matrix to monolayer graphene, showing that the graphene acts as a reinforcing phase. Graphene-like metal nanocomposites represent one of the most technologically promising developments of high-performance material systems.

Roman and Cranford [126] evaluated the mechanical properties of graphdiyne–copper nanocomposites, combining varied numbers of layers of graphdiyne sheets on copper substrate, as well as sandwich-structured copper/graphdiyne layers (see Figure 8.14(a)–(d)).

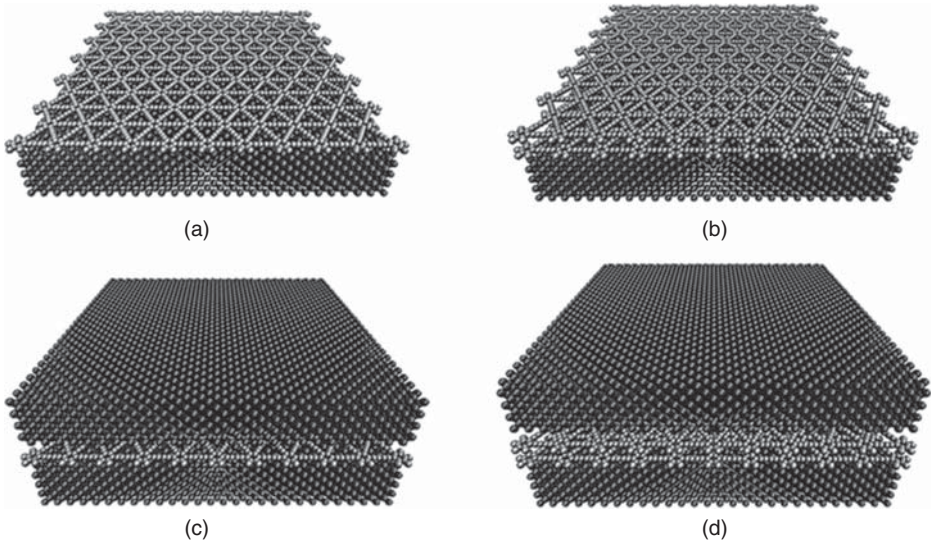

Figure 8.14 Nanocomposite configurations: (a) single graphdiyne with copper substrate, (b) bilayer graphdiyne with copper substrate, (c) single graphdiyne with copper sandwich, (d) bilayer graphdiyne with copper sandwich. [126]

Using full atomistic MD, the elastic stiffness, toughness, and limit states of these nanocomposite materials were explored considering an atomistically large model at finite temperature through direct tensile loads, using defect-free and defective copper substrates. The nature of the bonding interaction between the copper and graphdiyne is noncovalent; therefore, there is no energetic cost to bond the composite. The results show that a relatively slight amount of graphdiyne can dramatically increase the tensile strength and toughness of copper, although it is only a single atomic layer in thickness, representing nominal increases in both system size and weight. Also, it is demonstrated that combining copper with layers of graphdiyne can increase substantially the failure strain by confining the copper crystal during deformation. More interestingly is the effect on the copper component in the composite – the graphdiyne allows the copper to carry stress as if the imperfections were not present. This strengthening mechanism (e.g., constraining dislocations) acts in combination with classical rule-of-mixture enhancements (e.g., proportional stiffness) such that the contribution of copper is near-optimal in the composite system – graphdiyne improves the response of the composite material [126].

Proving the applicability of continuum mechanics, including micromechanics, to composites at the atomic level, many recent works have reported that continuum mechanics can be employed to analyze the behavior of nanocomposites. The well-known rule of mixture (RoM) for composites can be utilized to predict the tensile modulus of the nanocomposites. The modulus of the composite, $Y_{composites}$, can be calculated from the equation:

$$Y_{\text{composite}} = \frac{1}{V}\sum\nolimits_i Y_i V_i = Y_{2D} n_{2D} + Y_{\text{matrix}} n_{\text{matrix}} \tag{8.54}$$

where Y_{2D} is the tensile modulus of the 2D nanostructure sheet, Y_{matrix} is the tensile modulus of the matrix, n_{2D} and n_{matrix} are the volume fractions ($n_i = V_i/V$) of the 2D nanostructure sheet and matrix, respectively. Equation (8.54) can be extended to any two-phase composites, regardless the shape of the reinforcement. Note that in these formulas, only three parameters are involved, that is, modulus of the 2D nanomaterial layer and the matrix, and the volume fraction [2, 126]. Similarly, Gong et al. [125] have modeled the behavior of graphene monolayer nanocomposites using shear-lag theory, where it is assumed that the graphene is a mechanical continuum and surrounded by a layer of elastic polymer resin, and that there is an elastic stress transfer from the matrix to the graphene layer through a shear stress at the graphene–matrix interface. For a given level of matrix strain, e_m, it is predicted that the variation of strain in the graphene monolayer, e_f, with position, x, across the monolayer will be of the form:

$$e_f = e_m\left[1 - \frac{\cos h\left(ns\frac{x}{l}\right)}{\cos h\left(\frac{ns}{2}\right)}\right] \tag{8.55}$$

where

$$n = \sqrt{\frac{2G_m}{E_g}\left(\frac{t}{T}\right)} \tag{8.56}$$

and G_m is the matrix shear modulus, E_f is the Young's modulus of the graphene flake, l is the length of the graphene flake in the x direction, t is the thickness of the graphene, T is the total resin thickness, and s is the aspect ratio of the graphene (l/t) in the x-direction. The parameter n is widely accepted in composite micromechanics to be an effective measure of the interfacial

stress transfer efficiency, so *ns* depends on both the morphology of the graphene monolayer and the degree of interaction it has with the matrix. The variation of shear stress, τ_i, at the polymer graphene interface is given by

$$\tau_i = nE_g e_m \left[\frac{\sin h\left(ns\frac{x}{l}\right)}{\cos h\left(\frac{ns}{2}\right)} \right] \tag{8.57}$$

Reviewing these equations, it can be noted that the graphene monolayer is subjected to the highest level of stress, when the value of the product n_s is high. This implies that for good reinforcement a high aspect ratio, *s*, is desirable along with a high value of *n*. This analysis relies on the assumption that both the graphene monolayer and polymer behave as linear elastic continua [2, 125, 127].

8.7 Conclusion

Herein, we have discussed the emergence of 2D materials and the basic mechanical characterization thereof. Clearly then, the importance of graphene is not only that it has unique properties but also that it has paved the way for, and promoted interest in, the isolation and synthesis of many other 2D materials. We can now talk about a whole new class of materials, 2D atomic crystals, and already have examples with a large variety of properties (from large band-gap insulators to the very best conductors, the extremely mechanically strong to the soft and fragile, and the chemically active to the very inert). Furthermore, many of the properties of these 2D materials are very different from those of their 3D counterparts, leading to interesting discoveries in previously assumed 3D crystals (e.g., silicon to silicene). Because of their unique properties, 2D materials have attracted significant interest for both fundamental research and practical applications. In addition to the research on individual graphene-like 2D materials, a lot of effort has also been focused on the creation of multilayered heterostructures and composites as well. With most of these extraordinary materials characterized, experimentally and theoretically, we are getting to the point of convergence where the focus will be to turn these wonder properties in useful applications. The mechanical behavior of such materials is intriguing, acting as both crystals in membranes, requiring prudence in assigning traditional properties such as a Young's modulus (e.g., in MPa or N-m). Indeed, many of the low hanging fruits of these materials – characterizing and investigating the fundamental mechanical properties as discussed – have been harvested. At the same time, in terms of their material potential in future technological applications, we have merely scratched the 2D surface.

Acknowledgment

N.M.P. is supported by the European Research Council (ERC StG Ideas 2011 BIHSNAM No. 279985 on Bio-Inspired hierarchical supernanomaterials, ERC PoC 2013-1 REPLICA2 No. 619448 on Largearea replication of biological antiadhesive nanosurfaces, ERC PoC 2013-2 KNOTOUGH No. 632277 on Supertough knotted fibers), by the European Commission under the Graphene Flagship (WP10 "Nanocomposites," No. 604391) and by the Provincia Autonoma di Trento ("Graphene Nanocomposites," No. S116/2012-242637 and delib. reg. No. 2266).

References

[1] Novoselov, K.S. et al. (2004) Electric field effect in atomically thin carbon films. *Science*, **306**, 666–669.

[2] Hu, H., Onyebueke, L. and Abatan, A. (2010) Characterizing and modeling mechanical properties of nanocomposites: Review and evaluation. *Journal of Minerals and Materials Characterization and Engineering*, **9** (4), 275–319.

[3] Miro, P., Audiffred, M. and Heine, T. (2014) An atlas of two-dimensional materials. *Chemical Society Reviews*, **43** (18), 6537–6554.

[4] Tang, Q., Zhou, Z. and Chen, Z. (2013) Graphene-related nanomaterials: Tuning properties by functionalization. *Nanoscale*, **5** (11), 4541–4583.

[5] Lee, C., Wei, X., Kysar, J.W. and Hone, J. (2008) Measurement of the elastic properties and intrinsic strength of monolayer graphene. *Science*, **321**, 385–388.

[6] Koenig, S.P., Boddeti, N.G., Dunn, M.L. and Bunch, J.S. (2011) Ultrastrong adhesion of graphene membranes. *Nature Nanotechnology*, **6**, 543–546.

[7] Sen, D. et al. (2010) Tearing graphene sheets from adhesive substrates produces tapered nanoribbons. *Small*, **6** (10), 1108–1116.

[8] Haley, M.M., Brand, S.C. and Pak, J.J. (1997) Carbon networks based on dehydrobenzoannulenes: Synthesis of graphdiyne substructures. *Angewandte Chemie International Edition in English*, **36** (8), 836–838.

[9] Li, G. et al. (2010) Architecture of graphdiyne nanoscale films. *Chemical Communications (Cambridge, England)*, **46** (19), 3256–3258.

[10] Ivanovskii, A.L. (2013) Graphynes and graphdyines. *Progress in Solid State Chemistry*, **41** (1-2), 1–19.

[11] Cranford, S.W., Brommer, D.B. and Buehler, M.J. (2012) Extended graphynes: Simple scaling laws for stiffness, strength and fracture. *Nanoscale*, **4** (24), 7797–7809.

[12] Enyashin, A.N. and Ivanovskii, A.L. (2011) Graphene allotropes. *Physica Status Solidi*, **248** (8), 1879–1883.

[13] Takeda, K. and Shiraishi, K. (1994) Theoretical possibility of stage corrugation in Si and Ge analogs of graphite. *Physical Review B*, **50** (20), 14916–14922.

[14] Guzman-Verri, G.G. and Voon, L.C.L.Y. (2007) Electronic structure of silicon-based nanostructures. *Physical Review B*, **76** (7), 075131.

[15] Tsai, W.-F. et al. (2013) Gated silicene as a tunable source of nearly 100% spin-polarized electrons. *Nature Communications*, **4**, 1500.

[16] Roman, R.E. and Cranford, S.W. (2014) Mechanical properties of silicene. *Computational Materials Science*, **82**, 50–55.

[17] Le, M.Q. and Nguyen, D.T. (2014) The role of defects in the tensile properties of silicene. *Applied Physics A*, **118**, 1437–1445.

[18] Song, L. et al. (2010) Large scale growth and characterization of atomic hexagonal boron nitride layers. *Nano Letters*, **10** (8), 3209–3215.

[19] Tang, Q. and Zhou, Z. (2013) Graphene-analogous low-dimensional materials. *Progress in Materials Science*, **58**, 1244–1315.

[20] Kostoglou, N., Polychronopoulou, K. and Rebholz, C. (2015) Thermal and chemical stability of hexagonal boron nitride (h-BN) nanoplatelets. *Vacuum*, **112**, 42–45.

[21] Peng, Q. et al. (2012) Elastic properties of hybrid graphene/boron nitride monolayer. *Acta Mechanica*, **223** (12), 2591–2596.

[22] Yue, Q. et al. (2012) Mechanical and electronic properties of monolayer MoS2 under elastic strain. *Physics Letters A*, **376** (12–13), 1166–1170.

[23] Dang, K.Q., Simpson, J.P. and Spearot, D.E. (2014) Phase transformation in monolayer molybdenum disulphide (MoS2) under tension predicted by molecular dynamics simulations. *Scripta Materialia*, **76**, 41–44.

[24] Peng, Q. and De, S. (2013) Outstanding mechanical properties of monolayer MoS2 and its application in elastic energy storage. *Physical Chemistry Chemical Physics*, **15** (44), 19427–19437.

[25] Gan, Y. and Zhao, H. (2014) Chirality effect of mechanical and electronic properties of monolayer MoS2 with vacancies. *Physics Letters A*, **378** (38–39), 2910–2914.

[26] Balendhran, S. et al. (2014) Elemental analogues of graphene: Silicene, germanene, stanene, and phosphorene. *Small*, **11**, 640–652.

[27] Cahangirov, S. et al. (2009) Two- and one-dimensional honeycomb structures of silicon and germanium. *Physical Review Letters*, **102** (23), 236804.

[28] Bianco, E. et al. (2013) Stability and exfoliation of germanane: A germanium graphane analogue. *ACS Nano*, **7** (5), 4414–4421.

[29] Li, L. et al. (2014) Buckled Germanene Formation on Pt(111). *Advanced Materials*, **26** (28), 4820–4824.
[30] van den Broek, B. et al. (2014) Two-dimensional hexagonal tin: ab initio geometry, stability, electronic structure and functionalization. *2D Materials*, **1** (2), 021004.
[31] Manjanath, A., Kumar, V. and Singh, A.K. (2014) Mechanical and electronic properties of pristine and Ni-doped Si, Ge, and Sn sheets. *Physical Chemistry Chemical Physics*, **16** (4), 1667–1671.
[32] Brent, J.R. et al. (2014) Production of few-layer phosphorene by liquid exfoliation of black phosphorus. *Chemical Communications*, **50** (87), 13338–13341.
[33] Lange, S., Schmidt, P. and Nilges, T. (2007) Au3SnP7@black phosphorus: An easy access to black phosphorus. *Inorganic Chemistry*, **46** (10), 4028–4035.
[34] Koski, K.J. and Cui, Y. (2013) The new skinny in two-dimensional nanomaterials. *ACS Nano*, **7** (5), 3739–3743.
[35] Li, Y. et al. (2014) Mechanical properties of hydrogen functionalized graphene allotropes. *Computational Materials Science*, **83**, 212–216.
[36] Zhao, H. (2012) Strain and chirality effects on the mechanical and electronic properties of silicene and silicane under uniaxial tension. *Physics Letters A*, **376** (46), 3546–3550.
[37] Leggett, G.J. (2009) Scanning probe microscopy, in *Surface Analysis – The Principal Techniques*, John Wiley & Sons, pp. 479–562.
[38] Cao, G. (2004) *Nanostructures and Nanomaterials – Synthesis, Properties and Applications*, World Scientific.
[39] Frank, I.W. et al. (2007) Mechanical properties of suspended graphene sheets. *Journal of Vacuum Science & Technology B*, **25** (6), 2558–2561.
[40] Ferralis, N. (2010) Probing mechanical properties of graphene with Raman spectroscopy. *Journal of Materials Science*, **45** (19), 5135–5149.
[41] Wang, H., Liu, F., Fu, W. et al. (2014) Two-dimensional heterostructures: Fabrication, characterization, and application. *Nanoscale*, **6**, 12250–12272.
[42] Bertolazzi, S., Brivio, J. and Kis, A. (2011) Stretching and breaking of ultrathin MoS2. *ACS Nano*, **5** (12), 9703–9709.
[43] Poot, M. and van der Zant, H.S.J. (2008) Nanomechanical properties of few-layer graphene membranes. *Applied Physics Letters*, **92** (6), 063111.
[44] Vogt, P. et al. (2012) Silicene: Compelling experimental evidence for graphenelike two-dimensional silicon. *Physical Review Letters*, **108** (15), 155501.
[45] Gouadec, G. and Colomban, P. (2007) Raman Spectroscopy of nanomaterials: How spectra relate to disorder, particle size and mechanical properties. *Progress in Crystal Growth and Characterization of Materials*, **53** (1), 1–56.
[46] Dresselhaus, M.S. et al. (2010) Perspectives on carbon nanotubes and graphene raman spectroscopy. *Nano Letters*, **10** (3), 751–758.
[47] Butler, S.Z. et al. (2013) Progress, challenges, and opportunities in two-dimensional materials beyond graphene. *ACS Nano*, **7** (4), 2898–2926.
[48] Nguyen, B.-S., Lin, J.-F. and Perng, D.-C. (2014) Microstructural, electrical, and mechanical properties of graphene films on flexible substrate determined by cyclic bending test. *ACS Applied Materials & Interfaces*, **6** (22), 19566–19573.
[49] Frenkel, D. and Smit, B. (2002) Molecular dynamics simulations, in *Understanding Molecular Simulation*, Second edn (eds D. Frenkel and B. Smit), Academic Press, San Diego, pp. 63–107.
[50] Cranford, S.W. and Buehler, M.J. (2012) *Biomateriomics*, Springer.
[51] Tsai, D.H. (1979) The virial theorem and stress calculation in molecular dynamics. *The Journal of Chemical Physics*, **70** (3), 1375–1382.
[52] Zimmerman, J.A. et al. (2004) Calculation of stress in atomistic simulation. *Modelling and Simulation in Materials Science and Engineering*, **12** (4), S319.
[53] Lu, Q., Gao, W. and Huang, R. (2011) Atomistic simulation and continuum modeling of graphene nanoribbons under uniaxial tension. *Modelling and Simulation in Materials Science and Engineering*, **19** (5), 054006.
[54] Huang, Y., Wu, J. and Hwang, K.C. (2006) Thickness of graphene and single-wall carbon nanotubes. *Physical Review B*, **74** (24), 245413.
[55] Baughman, R.H., Eckhardt, H. and Kertesz, M. (1987) Structure-property predictions for new planar forms of carbon: Layered phases containing sp2 and sp atoms. *The Journal of Chemical Physics*, **87** (11), 6687.
[56] Wei, X. et al. (2009) Nonlinear elastic behavior of graphene: *Ab initio* calculations to continuum description. *Physical Review B*, **80** (20), 205407.
[57] Lu, Q. and Huang, R. (2009) Nonlinear mechanical properties of graphene nanoribbons. *International Journal of Applied Mechanics*, **1** (3), 443–467.

[58] Zhou, J. and Huang, R. (2008) Internal lattice relaxation of single-layer graphene under in-plane deformation. *Journal of the Mechanics and Physics of Solids*, **56** (4), 1609–1623.
[59] Scarpa, F., Adhikari, S. and Phani, A.S. (2009) Effective elastic mechanical properties of single layer graphene sheets. *Nanotechnology*, **20** (6), 065709.
[60] Nasdala, L. and Ernst, G. (2005) Development of a 4-node finite element for the computation of nano-structured materials. *Computational Materials Science*, **33** (4), 443–458.
[61] Cranford, S.W. and Buehler, M.J. (2011) Mechanical properties of graphyne. *Carbon*, **49** (13), 4111–4121.
[62] Yang, Y. and Xu, X. (2012) Mechanical properties of graphyne and its family – A molecular dynamics investigation. *Computational Materials Science*, **61**, 83–88.
[63] Fasolino, A., Los, J.H. and Katsnelson, M.I. (2007) Intrinsic ripples in graphene. *Nature Materials*, **6** (11), 858–861.
[64] Kim, E.-A. and Neto, A.H.C. (2008) Graphene as an electronic membrane. *EPL*, **84** (5), 57007.
[65] Cranford, S., Sen, D. and Buehler, M.J. (2009) Meso-origami: Folding multilayer graphene sheets. *Applied Physics Letters*, **95** (12), 123121.
[66] Lu, Q., Arroyo, M. and Huang, R. (2009) Elastic bending modulus of monolayer graphene. *Journal of Physics D: Applied Physics*, **42** (10), 102002.
[67] Bunch, J.S. et al. (2007) Electromechanical resonators from graphene sheets. *Science*, **315** (5811), 490–493.
[68] Wang, X.L. et al. (2009) First-principles study on the enhancement of lithium storage capacity in boron doped graphene. *Applied Physics Letters*, **95** (18), 183103.
[69] Shi, Z.W. et al. (2012) Studies of graphene-based nanoelectromechanical switches. *Nano Research*, **5** (2), 82–87.
[70] Li, X.S. et al. (2009) Large-area synthesis of high-quality and uniform graphene films on copper foils. *Science*, **324** (5932), 1312–1314.
[71] Novoselov, K.S. et al. (2005) Two-dimensional atomic crystals. *Proceedings of the National Academy of Sciences of the United States of America*, **102** (30), 10451–10453.
[72] Hod, O. (2012) Graphite and hexagonal boron-nitride have the same interlayer distance. Why? *Journal of Chemical Theory and Computation*, **8** (4), 1360–1369.
[73] Zong, Z. et al. (2010) Direct measurement of graphene adhesion on silicon surface by intercalation of nanoparticles. *Journal of Applied Physics*, **107** (2), 026104.
[74] Wan, K.T. and Mai, Y.W. (1996) Fracture mechanics of a shaft-loaded blister of thin flexible membrane on rigid substrate. *International Journal of Fracture*, **74** (2), 181–197.
[75] Lu, Z.X. and Dunn, M.L. (2010) van der Waals adhesion of graphene membranes. *Journal of Applied Physics*, **107** (4), 044301.
[76] Sachs, B. et al. (2011) Adhesion and electronic structure of graphene on hexagonal boron nitride substrates. *Physical Review B*, **84** (19), 195414.
[77] Yi, L.J. et al. (2014) Temperature-induced unfolding of scrolled graphene and folded graphene. *Journal of Applied Physics*, **115** (20), 204307.
[78] Kim, K. et al. (2011) Multiply folded graphene. *Physical Review B*, **83** (24), 245433.
[79] Meng, X.H. et al. (2013) Mechanics of self-folding of single-layer graphene. *Journal of Physics D: Applied Physics*, **46** (5), 055308.
[80] Meng, X.H. et al. (2014) Folding of multi-layer graphene sheets induced by van der Waals interaction. *Acta Mechanica Sinica*, **30** (3), 410–417.
[81] Le, N.B. and Woods, L.M. (2012) Folded graphene nanoribbons with single and double closed edges. *Physical Review B*, **85** (3), 035403.
[82] Son, Y.W., Cohen, M.L. and Louie, S.G. (2006) Energy gaps in graphene nanoribbons. *Physical Review Letters*, **97** (21), 216803.
[83] Nakada, K. et al. (1996) Edge state in graphene ribbons: Nanometer size effect and edge shape dependence. *Physical Review B*, **54** (24), 17954–17961.
[84] Ritter, K.A. and Lyding, J.W. (2009) The influence of edge structure on the electronic properties of graphene quantum dots and nanoribbons. *Nature Materials*, **8** (3), 235–242.
[85] Zheng, Y.P. et al. (2011) Mechanical properties of grafold: A demonstration of strengthened graphene. *Nanotechnology*, **22** (47), 405701.
[86] Cranford, S.W. and Buehler, M.J. (2011) Packing efficiency and accessible surface area of crumpled graphene. *Physical Review B*, **84** (20), 205451.
[87] Zang, J.F. et al. (2013) Multifunctionality and control of the crumpling and unfolding of large-area graphene. *Nature Materials*, **12** (4), 321–325.

[88] Becton, M., Zhang, L.Y. and Wang, X.Q. (2014) Mechanics of graphyne crumpling. *Physical Chemistry Chemical Physics*, **16** (34), 18233–18240.
[89] Chen, Y., Lu, J. and Gao, Z.X. (2007) Structural and electronic study of nanoscrolls rolled up by a single graphene sheet. *Journal of Physical Chemistry C*, **111** (4), 1625–1630.
[90] Wang, Y. et al. (2015) Formation of carbon nanoscrolls from graphene nanoribbons: A molecular dynamics study. *Computational Materials Science*, **96**, 300–305.
[91] Xia, D. et al. (2010) Fabrication of carbon nanoscrolls from monolayer graphene. *Small*, **6** (18), 2010–2019.
[92] Xie, X. et al. (2009) Controlled fabrication of high-quality carbon nanoscrolls from monolayer graphene. *Nano Letters*, **9** (7), 2565–2570.
[93] Shi, X.H., Yin, Q.F. and Wei, Y.J. (2012) A theoretical analysis of the surface dependent binding, peeling and folding of graphene on single crystal copper. *Carbon*, **50** (8), 3055–3063.
[94] Chen, X.M. et al. (2014) Graphene folding on flat substrates. *Journal of Applied Physics*, **116** (16), 164301.
[95] Kwan, K. and Cranford, S.W. (2014) Scaling of the critical free length for progressive unfolding of self-bonded graphene. *Applied Physics Letters*, **104** (20), 203101.
[96] Zhang, L.Y., Zeng, X.W. and Wang, X.Q. (2013) Programmable hydrogenation of graphene for novel nanocages. *Scientific Reports*, **3**, 3162.
[97] Zhang, J. et al. (2010) Free folding of suspended graphene sheets by random mechanical stimulation. *Physical Review Letters*, **104** (16), 166805.
[98] Hiura, H. et al. (1994) Role of Sp(3) defect structures in graphite and carbon nanotubes. *Nature*, **367** (6459), 148–151.
[99] Pugno, N.M. (2006) Dynamic quantized fracture mechanics. *International Journal of Fracture*, **140** (1-4), 159–168.
[100] Pugno, N. (2006) New quantized failure criteria: Application to nanotubes and nanowires. *International Journal of Fracture*, **141** (1–2), 313–323.
[101] Pugno, N.M. and Ruoff, R.S. (2004) Quantized fracture mechanics. *Philosophical Magazine*, **84** (27), 2829–2845.
[102] Ippolito, M. et al. (2006) Role of lattice discreteness on brittle fracture: Atomistic simulations versus analytical models. *Physical Review B*, **73** (10), 104111.
[103] Taylor, D., Cornetti, P. and Pugno, N. (2005) The fracture mechanics of finite crack extension. *Engineering Fracture Mechanics*, **72** (7), 1021–1038.
[104] Pugno, N. et al. (2006) A generalized Paris' law for fatigue crack growth. *Journal of the Mechanics and Physics of Solids*, **54** (7), 1333–1349.
[105] Pugno, N., Cornetti, P. and Carpinteri, A. (2007) New unified laws in fatigue: From the Wöhler's to the Paris' regime. *Engineering Fracture Mechanics*, **74** (4), 595–601.
[106] Rice, J.R. and Rosengren, G.F. (1968) Plane strain deformation near a crack tip in a power-law hardening material. *Journal of the Mechanics and Physics of Solids*, **16** (1), 1–12.
[107] Carpinteri, A. and Pugno, N. (2005) Fracture instability and limit strength condition in structures with re-entrant corners. *Engineering Fracture Mechanics*, **72** (8), 1254–1267.
[108] Carpinteri, A. and Chiaia, B. (1986) Crack-resistance behavior as a consequence of self-similar fracture topologies. *International Journal of Fracture*, **76** (4), 327–340.
[109] Pugno, N.M. (2007) Young's modulus reduction of defective nanotubes. *Applied Physics Letters*, **90** (4), 043106.
[110] Pugno, N.M. and Ruoff, R.S. (2006) Nanoscale Weibull statistics. *Journal of Applied Physics*, **99** (2), 024301.
[111] Beale, P.D. and Srolovitz, D.J. (1988) Elastic fracture in random materials. *Physical Review B*, **37** (10), 5500–5507.
[112] Pugno, N.M. (2010) The design of self-collapsed super-strong nanotube bundles. *Journal of the Mechanics and Physics of Solids*, **58** (9), 1397–1410.
[113] Pugno, N. M., Yin, Q., Shi, X., Capozza, R., (2013) *A generalization of the Coulomb's friction law: from graphene to macroscale. Meccanica*, **48**, 1845–1851.
[114] Pugno, N.M. (2007) The role of defects in the design of space elevator cable: From nanotube to megatube. *Acta Materialia*, **55** (15), 5269–5279.
[115] Pugno, N.M. (2007) Space elevator: out of order? *Nano Today*, **2** (6), 44–47.
[116] Pugno, N.M. (2006) On the strength of the carbon nanotube-based space elevator cable: From nanomechanics to megamechanics. *Journal of Physics: Condensed Matter*, **18** (33), S1971.
[117] Jiang, J.W. and Park, H.S. (2014) Mechanical properties of MoS_2/graphene heterostructures. *Applied Physics Letters*, **105** (3), 033108.

[118] Giovannetti, G. et al. (2007) Substrate-induced band gap in graphene on hexagonal boron nitride: *Ab initio* density functional calculations. *Physical Review B*, **76** (7), 073103.
[119] Kaloni, T.P., Cheng, Y.C. and Schwingenschlogl, U. (2012) Electronic structure of superlattices of graphene and hexagonal boron nitride. *Journal of Materials Chemistry*, **22** (3), 919–922.
[120] Sakai, Y., Koretsune, T. and Saito, S. (2011) Electronic structure and stability of layered superlattice composed of graphene and boron nitride monolayer. *Physical Review B*, **83** (20), 205434.
[121] Zhong, X. et al. (2012) Electronic structure and quantum transport properties of trilayers formed from graphene and boron nitride. *Nanoscale*, **4** (17), 5490–5498.
[122] Ramasubramaniam, A., Naveh, D. and Towe, E. (2011) Tunable band gaps in bilayer graphene−BN heterostructures. *Nano Letters*, **11** (3), 1070–1075.
[123] Li, Y.-J. et al. (2012) Hexagonal boron nitride intercalated multi-layer graphene: A possible ultimate solution to ultra-scaled interconnect technology. *AIP Advances*, **2** (1), 012191.
[124] Kim, Y. et al. (2013) Strengthening effect of single-atomic-layer graphene in metal-graphene nanolayered composites. *Nature Communications*, **4**, 2114.
[125] Gong, L., Kinloch, I.A., Young, R.J. et al. (2010) Interfacial stress transfer in a graphene monolayer nanocomposite. *Advanced Materials*, **22**, 2694–2697.
[126] Roman, R.E. and Cranford, S.W. (2014) Strength and toughness of graphdiyne/copper nanocomposites. *Advanced Engineering Materials*, **16** (7), 862–871.
[127] Young, R.J., Kinloch, I.A., Gong, L. and Novoselov, K.S. (2012) The mechanics of graphene nanocomposites: A review. *Composites Science and Technology*, **72**, 1459–1476.